2016

Towards quantifying the effects of resource extraction on land cover and topography through remote sensing analysis: Confronting issues of scale and data scarcity

Jessica D. DeWitt

Towards quantifying the effects of resource extraction on land cover and topography through remote sensing analysis: confronting issues of scale and data scarcity

Jessica D. DeWitt

Dissertation submitted to the Eberly College of Arts and Sciences
at West Virginia University
in partial fulfillment of the requirements
for the degree of

Doctor of Philosophy

in

Geography

Timothy A. Warner, Committee Chairperson
J. Steven Kite, Ph.D.
Rick E. Landenberger, Ph.D.
Brenden E. McNeil, Ph.D.
Nicolas P. Zegre, Ph.D.

Geology & Geography

Morgantown, West Virginia

2016

Keywords:

ABSTRACT

Towards quantifying the effects of resource extraction on land cover and topography through remote sensing analysis: confronting issues of scale and data scarcity

Jessica D. DeWitt

This dissertation focuses on the mapping and monitoring of mineral mining activity using remotely sensed data. More specifically, it explores the challenges and issues associated with remote sensing-based analysis of land use land cover (LULC) and topographic changes in the landscape associated with artisanal and industrial-scale mining. It explores broad themes of image analysis, including evaluation of error in digital elevation models (DEMs), integration of multiple scales and data sources, quantification of change, and remote sensing classification in data-scarce environments. The dissertation comprises three case studies.

The first case study examines the LULC change associated with two scales of mining activity (industrial and artisanal) near Tortiya, Côte d'Ivoire. Industrial mining activity was successfully mapped in a regional LULC classification using Landsat multispectral imagery and support vector machines (SVMs). However, mapping artisanal mining required high-resolution imagery to discriminate the small, complex patterns of associated disturbance.

The second case study is an investigation of the potential for quantifying topographic change associated with mountain top removal mining and the associated valley-fill operations for a region in West Virginia, USA, using publically available DEMs. A 1:24,000 topographic map data, the shuttle radar topography mission (SRTM) DEM, a state-wide photogrammetric DEM, and the Advanced Spaceborne Thermal Emission Radiometer (ASTER) Global DEM (GDEM) were compared to a lidar bare-earth reference DEM. The observed mean error in both the SRTM and GDEM was statistically different than zero and modeled a surface well above the reference DEM surface. Mean error in the other DEMs was lower, and not significantly different than zero. The magnitude of the root mean square error (RMSE) suggests that only topographic change associated with the largest topographic disturbances would be separable from background noise using global DEMS such as the SRTM. Nevertheless, regionally available DEMs from photogrammetric sources allow mapping of mining change and quantification of the total volume of earth removal.

Monitoring topographic change associated with mining is challenging in regions where publically available DEMs are limited or not available. This challenge is particularly acute for artisanal mining, where the topographic disturbance, though locally important, is unlikely to be detected in global elevation data sets. Therefore, the third and final case study explored the potential for creating fine-spatial resolution bare-earth DEMs from digital surface models (DSMs) using high spatial resolution commercial satellite imagery and subsequent filtering of elevation artifacts using commercial lidar software and other spatial filtering techniques. Leaf-on and leaf-off DSMs were compared to highlight the effect of vegetation on derived bare-earth DEM accuracy. The raw leaf-off DSM was found to have very low error overall, with notably higher error in areas of evergreen vegetation. The raw leaf-on DSM was found to have a RMSE error much higher than the leaf-off data, and similar to that of the SRTM in dense deciduous forest. However, filtering using the commercial techniques developed for lidar notably reduced the error present in the raw DSMs, suggesting that such approaches could help overcome data scarcity in regions where regional or national elevation data sets are not available.

Collectively this research addressed data issues and methodological challenges in the analysis of 3D changes caused by resource extraction. Elevation and optical imagery are key data sets for mapping the disturbance associated with mining. The particular combination required regarding data spatial scale, and for elevation, accuracy, is a function of the type and scale of the mining.

Table of Contents

Chapter 1 Introduction

Mineral resource extraction is of central importance for much of our current society and culture, and we live in a world that increasingly relies upon the wide variety of products that are produced from minerals such as iron, aluminum, tin, copper, and coal (EEA 2005, Otto 1997, Robinson 1998). Although coal is not chemically classified as a mineral, within the mining industry it is referred to as a 'fuel mineral' due to the type of its deposits and associated methods of mining (Spitz and Trudinger 2008). The mining of mineral resources includes all activities related to excavating the minerals and ore, which can be sold at a profit. Such activity can have a significant economic impact on both the host country and internationally. Mining activity also has benefits and associated risks for to the immediate locale, and may result in substantial changes to the environment and local economy (Hartman 1992, Spitz and Trudinger 2008). Response to these changes can take a variety of forms, many of which require baseline mapping through remote sensing (Spitz and Trudinger 2008). Mapping and monitoring of mine sites is also important to allow for quantification of change over time.

Mining activities occur at vastly different scales, from artisanal small-scale mining to large-scale industrial mining, and via different methods, including surface, underground and solution mining, depending on the type of mineral and its deposit characteristics (Spitz and Trudinger 2008). However, a majority of minerals are extracted through large-scale surface mining, wherein sizeable volumes of overburden and waste material are removed from the landscape to reveal near-surface mineral deposits (Hartman 1992). The overburden and waste material are typically deposited nearby, either filling in the previously mined area or in the form of a spoil pile. Surface mining is one of the most cited examples of humans acting as geomorphic agents of change (Hooke 1994, Kite 1999, Kite 2009), as it can result in significant and enduring changes to both the land cover and the topography of a region. These changes can cause a wide variety of environmental concerns, including geochemical degradation to groundwater resources (Orem et al. 2012), landslides and associated issues in surface stability (Sah, Sheorey, and Upadhyaya 1994), hydrologic flow changes (Negley and Eshleman 2006, Phillips 2004), and reduction in biodiversity as a result of habitat change (Maxwell et al. 2012), as well as other social and cultural degradations (Woodfork et al. 2001). Artisanal and small-scale mining (ASM) entails the extraction of near-surface mineral resources by individual or small groups of miners using primarily manual or low technology methods (Barry 1996, Hentschel 2002). Although a single artisanal mine pit may be small in spatial extent, artisanal mining activity of many individuals has the cumulative potential to cover large areas and result in significant land cover changes. Environmental impacts of artisanal mining depend on the extent and scale of the mining activity, but potentially include many of those relevant for industrial

mining, such as geochemical degradation of groundwater and hydrologic flow changes (Barry 1996, Hentschel 2002, Aryee, Ntibery, and Atorkui 2003). In addition to environmental effects, there are many social and political effects of ASM (Hentschel 2002, Chirico and Malpeli 2013).

As a general rule, remote sensing methods have been successfully implemented to map and monitor surficial mining (Townsend et al. 2009, Demirel 2011). Several studies have shown that surficial mining and associated land cover changes can be effectively mapped using remotely sensed multispectral imagery (Latifovic 2005, Schueler, Kuemmerle and Schröder 2011), despite the challenges suggested by Irons (1980). Moreover, the progression of mining LULC across a landscape can be monitored through an integrated analysis of multiple sources of remotely sensed imagery and other geospatial data for mapping of mine extent (Inglis et al. 1978). Remote sensing methods have also been used to investigate the environmental impacts associated with surface mining activity (Merriam et al. 2015, Choe 2008, Mars and Crowley 2003, Rathore 1993). However, the small spatial extent of an artisanal mining footprint makes it difficult to detect using imagery of moderate or coarse scale (Elmes et al. 2014). Some studies have successfully mapped ASM using high-resolution satellite imagery (Telmer and Stapper 2007, Pagot et al. 2008), however inaccuracy in the detail of mining-specific land use (such as active mining zones and transportation corridors or settlement areas) remains a challenge for automated mapping methods (Luethje et al. 2014).

More recent technological and data availability improvements have facilitated the mapping and quantification of topographic changes from industrial-scale mining (Gesch 2014, Lesniak and Porzycka 2008). In areas of industrial mining the incorporation of topographic changes, including volume estimates, has greatly improved the accuracy of environmental models of water quality and pollution (Ross, McGlynn and Bernhardt 2016). Although moderate-scale digital elevation models (DEMs) have been used to quantify topographic change in surface mined areas (Gesch 2005), the relative accuracy of such datasets calls into question the accuracy of the quantified change and the minimum amount of change that could be quantified using such methods (DeWitt 2015). Although a few studies have attempted to quantify topographic change at artisanal mine sites with mixed results (Emel, Plisinski and Rogan 2014), the success of this mapping is mixed due to the comparatively limited topographic changes that occur at such sites and the paucity of data in ASM locations (Aryee, Ntibery, and Atorkui 2003, and UNECA 2007), and ASM topographic change remains a current area of research. The necessary fine-spatial resolution and high-accuracy DEMs for densely vegetated regions would typically require lidar, however such data remain unavailable or infeasible to collect in remote areas of the globe. Note that in this dissertation, the terms ‘digital elevation model’ (DEM) and ‘digital surface model’ (DSM) will both

be used with respect to gridded elevation data. In this context, a DEM refers to an elevation model with z-values indicating the elevation of the bare-earth ground surface, devoid of any surface features. A DSM indicates an elevation model with z-values indicating the elevation of bare-earth ground surface plus the height of any surface features present in the same space (a surface also referred to as the 'reflective surface').

Thus, there are two interconnected themes regarding the remote sensing of mining: 1) the scale of mining as a factor determining the efficacy of remote sensing methods, and 2) the dimensionality of the remotely sensed quantification – whether identification of LULC extent, three dimensional analysis combining LULC with topography, or four dimensional (4D) analysis of LULC and topographic changes over time. The latter provides a more comprehensive understanding of the web of interrelated impacts and fallouts (Xie et al. 2005). More importantly, the inclusion of change over time in the analysis of mining effects provides actionable information for policy and management.

This dissertation focuses on the mapping and monitoring of mineral extraction sites over time using remote sensing methods, by exploring the challenges associated with remote sensing-based analysis of LULC and topographic changes from mining at the artisanal to the industrial-scale. Monitoring of mining at each of the scales is investigated and challenges to quantifying change over time are addressed. Another central theme of this work is of investigating LULC and topographic change in rural, international data-scarce environments. In these situations it is often necessary to devise new methods of integrating diverse datasets (chapter 2), or of establishing the methodological accuracy in areas of high data availability for use in data scarce areas (as in Chapter 4).

This dissertation comprises four chapters. The first chapter is this general introduction, which explains the context of the work, and the central research questions. Chapters 2-4 are outlined below. Chapter 5 is an overall conclusion, summarizing the contribution of the work.

Chapter 2 is titled "Integration of local- and regional-scale analysis of LULC change across 46 years using multi-source remote sensing methods in a post-conflict area of industrial and artisanal diamond mining." This chapter is focused on the question how fine-scale artisanal mining land use can be incorporated into a remote sensing analysis of regional-scale land cover changes, and in doing so provides an evaluation of this integration in the context of mapping and monitoring mining land use. The study area, in Côte d'Ivoire, is a region with only limited high-resolution data available. In such areas, moderate resolution data such as Landsat multispectral imagery is the best available geospatial data, but the small

spatial extent of ASM land use is difficult to capture in land cover classification at this spatial resolution. In this chapter, I therefore explore the possibilities for synthesizing fine-scale and regional-scale analysis with multiple datasets for analysis of changing ASM activities over multiple decades.

Chapter 3 is titled, "Comparison of DEMS derived from USGS DLG, SRTM, a statewide photogrammetry program, ASTER GDEM and lidar: implications for change detection." Given the availability of a growing number of global and, in some areas, regional, DEMs of different ages, Chapter 3 evaluates the potential to use such data to monitor and quantify topographic change associated with mountain top removal mining and the associated valley fill operations in West Virginia, USA. Specifically, the chapter investigates the comparability of currently available DEMs, and how effectively such DEMs can be combined to analyze topographic changes in mining areas. Key issues regarding the various source data, and the implications for uncertainty in modeling the topographic changes, are explored.

Chapter 4 is titled "Creating high-resolution bare earth digital elevation models (DEMs) from stereo imagery using lidar point cloud procedures in an area of densely vegetated deciduous forest." This chapter addresses methodological questions centered on digital surface models (DSMs) created photogrammetrically from high spatial resolution commercial satellite imagery of vegetated regions and how such DSMs can be manipulated to produce elevation rasters that approximate bare-earth DEMs. The ability to generate multiple high-resolution bare-earth DEMs over time from commercial imagery would offer the promise of monitoring the fine scale changes associated ASM, even in areas of limited data availability, such as Côte d'Ivoire, the study area for Chapter 2. I hypothesize that lidar software filtering methods and other related techniques can be used to filter a photogrammetric DSM to produce a DEM. I also investigate whether accurate DEMS can be produced from high-resolution imagery in leaf-off periods, or whether the bare trees and their shadows create noise in the data set. The study site for this chapter, a park in Woodbridge, Virginia, USA, was chosen because of the presence of a closed canopy forest and also the availability of excellent control data, in the form of a lidar dataset.

References

Aryee, B., B. Ntibery, and E. Atorkui. 2003. Trends in the Small-Scale Mining of Precious Minerals in Ghana: A Perspective on Its Environmental Impact. Journal of Cleaner Production 11 (2): 131–40. doi:10.1016/S0959-6526(02)00043-4.

Asner, G., W. Llactayo, R. Tupayachi, and E. Ráez. 2013. Elevated Rates of Gold Mining in the Amazon Revealed through High-Resolution Monitoring. Proceedings of the National Academy of Sciences 110 (46): 18454–59. doi:10.1073/pnas.1318271110.

Barry, M. 1996. Regularizing Informal Mining: A Summary of the Proceedings of the International Roundtable on Artisanal Mining. The World Bank, Industry and Energy Department Occasional Paper No. 6. Washington, D.C.

Chirico, P., and K. Malpeli. 2013. Reconnaissance Investigation of the Rough Diamond Resource Potential and Production Capacity of Côte D 'Ivoire. U.S. Geological Survey Scientific Investigations Report SIR 2013-5: 46.

Choe, E., F. van der Meer, F. van Ruitenbeek, H. van der Werff, B. de Smeth, and Y. Kim. 2008. "Mapping of Heavy Metal Pollution in Stream Sediments Using Combined Geochemistry, Field Spectroscopy, and Hyperspectral Remote Sensing: A Case Study of the Rodalquilar Mining Area, SE Spain." Remote Sensing of Environment 112 (7): 3222–33. doi:10.1016/j.rse.2008.03.017.

Demirel, N., M. Emil, and H. Duzgun. 2011. "Surface Coal Mine Area Monitoring Using Multi-Temporal High-Resolution Satellite Imagery." International Journal of Coal Geology 86 (1). Elsevier B.V.: 3–11. doi:10.1016/j.coal.2010.11.010.

DeWitt, J., T. Warner, and J. Conley. 2015. Comparison of DEMs derived from USGS DLG, SRTM, a statewide photogrammetry program, ASTER GDEM and LiDAR: implications for change detection. GIScience & Remote Sensing.

EEA. 2005. Sustainable Use and Management of Natural Resources, Report No 9/2005.

Elmes, A., J. Ipanaqué, J. Rogan, N. Cuba, and A. Bebbington. 2014. "Mapping Licit and Illicit Mining Activity in the Madre de Dios Region of Peru." Remote Sensing Letters 5 (10): 882–91. doi:10.1080/2150704X.2014.973080.

Emel, J., J. Plisinski, and J. Rogan. 2014. "Monitoring Geomorphic and Hydrologic Change at Mine Sites Using Satellite Imagery: The Geita Gold Mine in Tanzania." Applied Geography 54. Elsevier Ltd: 243–49. doi:10.1016/j.apgeog.2014.07.009.

Hartman, H., ed. 1992. SME Mining Engineering Handbook, Society for Mining, Metallurgy and Exploration, Inc. Littleton, CO. 2260p.

Gesch, D. 2005. "Analysis of Multi-Temporal Geospatial Data Sets to Assess the Landscape Effects of Surface Mining." In Proceedings of the 22nd Annual National Conference of the American Society of Mining and Reclamation, 19–23.

Gesch, D. 2014. “An Inventory of Topographic Surface Changes: The Value of Multi-Temporal Elevation Data for Change Analysis and Monitoring.” ISPRS - International Archives of the Photogrammetry, Remote Sensing and Spatial Information Sciences XL-4 (May): 59–63. doi:10.5194/isprsarchives-XL-4-59-2014.

Hentschel, T., F. Hruschka, and M. Priester. 2002. Global Report on Artisanal and Small-Scale Mining. Mining, Minerals and Sustainable Development. https://www.commdev.org/userfiles/files/804_file_global_report_on_artisanal.pdf.

Höhle, J., and M. Höhle. 2009. “Accuracy Assessment of Digital Elevation Models by Means of Robust Statistical Methods.” Isprs Journal of Photogrammetry and Remote Sensing 64: 398–406. doi:10.1016/j.isprsjprs.2009.02.003.

Hooke, R. 1994. "On the efficacy of humans as geomorphic agents." GSA Today 4(9): 217.

Inglis, M., H. Sheffer, R. Lyon, and A. Prelat. 1978. “Landsat Monitoring of the Navajo Coal Surface Mine.” In Proceedings of the American Society of Photogrammetry, fall techn:523–38.

Kite, J., and J. Skousen. 1999. “Scale and Morphology of Landforms Related to Coal Mining; Trends in Coalfields of the Appalachian Plateaus.” Abstracts with Programs - Geological Society of America 31 (7). Boulder, CO, United States (USA): Geological Society of America (GSA), Boulder, CO: 232.

Kite, S. 2009. “A Geomorphologiest’s Perspective on Stream and Watershed Restoration in the Appalachian Coal Fields.” In Geomorphic Reclamation and Natural Stream Design at Coal Mines: A Technical Interactive Forum, edited by K C Vories and A H Caswell, 3–12. Bristol, VA: U.S. Office for Surface Mining.

Kimberley Process website.Accessed Online at < https://www.kimberleyprocess.com/> on 17 Nov 2016.

Latifovic, R., K. Fytas, J. Chen, and J. Paraszczak. 2005. “Assessing Land Cover Change Resulting from Large Surface Mining Development.” International Journal of Applied Earth Observation and Geoinformation 7 (1): 29–48. doi:10.1016/j.jag.2004.11.003.

Lesniak, A., and S. Porzycka. 2008. “Comprehensive Interpretation of Satellite and Surface Measurements for Hazard Assessment on Mining and Post Mining Areas.” Gospodarka Surowcami Mineralnymi-Mineral Resources Management 24 (2): 147–59.

Luethje, F., O. Kranz, and E. Schoepfer. 2014. “Geographic Object-Based Image Analysis Using Optical Satellite Imagery and GIS Data for the Detection of Mining Sites in the Democratic Republic of the Congo.” Remote Sensing 6(7): 6636–6661. doi:10.3390/rs6076636.

Mars, J., and J. Crowley. 2003. “Mapping Mine Wastes and Analyzing Areas Affected by Selenium-Rich Water Runoff in Southeast Idaho Using AVIRIS Imagery and Digital Elevation Data.” Remote Sensing of Environment 84 (3): 422–36.

Maxwell, A., M. Strager, C. Yuill, and J. Petty. 2012. “Modeling Critical Forest Habitat in the Southern Coal Fields of West Virginia.” International Journal of Ecology, no. October 2016. doi:10.1155/2012/182683.

Merriam, E., J. Petty, M. Strager, A. Maxwell, and P. Ziemkiewicz. 2015. “Landscape-Based Cumulative Effects Models for Predicting Stream Response to Mountaintop Mining in Multistressor Appalachian Watersheds.” Freshwater Science 34 (3): 1006–19. doi:10.1086/681970.

Negley, T., and K. Eshleman. 2006. “Comparison of Stormflow Responses of Surface-Mined and Forested Watersheds in the Appalachian Mountain, USA.” Hydrological Processes 20: 3467–83.

Phillips, J. 2004. “Impacts of Surface Mine Valley Fills on Headwater Floods in Eastern Kentucky.” Environmental Geology 45: 367–80.

Orem, W., C. Tatu, L. Crosby, M. Varonka, A. Bates, M. Engle, N. Geboy, and M. Hendryx. 2012. “Water Chemistry in Areas with Surface Mining of Coal, West Virginia, Usa.” Abstracts with Programs - Geological Society of America 44 (7).

Otto, J. 1997. Mineral policy, legislation, and regulation; Mining, Environment and Development, UNCTAD.

Rathore, C, and R. Wright. 1993. “Monitoring Environmental Impacts of Surface Coal-Mining.” International Journal of Remote Sensing 14 (6): 1021–42.

Robinson, J., and J. Tinker. 1998. Reconciling Ecological, Economic, and social imperatives; In Schnurr J and S. Holtz eds., The Cornerstone of Development: Integrating Environmental, Social and Economic Policies, Ottawa: International Development Research Centre, pp9-44.

Ross, M., B. McGlynn, and E. Bernhardt. 2016. “Deep Impact: Effects of Mountaintop Mining on Surface Topography, Bedrock Structure, and Downstream Waters.” Environmental Science & Technology. 50: 2064-2074.

Sah, N., P. Sheorey, and L. Upadhyaya. 1994. “Maximum Likelihood Estimation of Slope Stability.” International Journal of Rock Mechanics and Mining Sciences & Geomechanics Abstracts 31 (1): 47–53. doi:http://dx.doi.org/10.1016/0148-9062(94)92314-0.

Schueler, V., T. Kuemmerle, and H. Schröder. 2011. “Impacts of Surface Gold Mining on Land Use Systems in Western Ghana.” Ambio. doi:10.1007/s13280-011-0141-9.

Spitz, K., and J. Trudinger, eds. 2008. Mining and the Environment. New York, NY: CRC Press Taylor & Francis Group. doi:10.1016/0301-4207(80)90036-7.

Telmer, K., and D. Stapper. 2007. “Evaluating and Monitoring Small Scale Gold Mining and Mercury Use: Building a Knowledge-Base with Satellite Imagery and Field Work.” UNIDO Project Final Report EG/GLO/01/G34. Victoria, BC.

Townsend, P., D. Helmers, C. Kingdon, B. McNeil, K. de Beurs, and K. Eshleman. 2009. “Changes in the Extent of Surface Mining and Reclamation in the Central Appalachians Detected Using a 1976-2006 Landsat Time Series.” Remote Sensing of Environment 113 (1): 62–72. doi:10.1016/j.rse.2008.08.012.

UNECA. 2007. “Determination Fundamental Datasets for Africa: GeoInformation In Socio-Economic Development.” UN Economic Commssion for Africa Report. Addis Ababa, Ethiopia.

Woodfork, L., S. McClelland, D. Newell, and A. Thomson. 2001. “Environmental, Economic, and Societal Impacts of Mountaintop Removal Mining (MRTM) in the Central Appalachians.” Abstracts with Programs - Geological Society of America 33 (6). Boulder, CO, United States (USA): Geological Society of America (GSA), Boulder, CO: 199

Xie, H., H. Hu, H. Jimg, Y. Gao, Q. Chen, and Z. Feng. 2005. “4D and Application of Land Reclamation in Mining Area.” Transactions of Nonferrous Metals Society of China 15 (March): 41–44.

Chapter 2 Integration of local- and regional-scale analysis of LULC change across 46 years using multi-source remote sensing methods in a post-conflict area of industrial and artisanal mining

Jessica D. DeWitt, Peter G. Chirico, Sarah E. Bergstresser, and Timothy A. Warner

Abstract

Since the closure of the industrial diamond mine in Tortiya, Côte d'Ivoire, artisanal and small-scale mining (ASM) has played a substantial role in the region's economy and culture, particularly through a period of violent political conflict. However in recent years other land uses, such as plantation-scale tree crops, have expanded exponentially in this mining region. Long-term land use land cover (LULC) mapping of trends in these and in other categories of LULC is required to allow for land use planning and to address the potential for land use conflicts. However, standard remote sensing multispectral LULC classification methodologies cannot adequately address the vastly different scales of economically and politically important land uses such as ASM and plantation tree crops. This study demonstrates a multi-source, multi-scalar data integration approach for mapping 46 years of LULC change in a region of widespread ASM and rapid expansion of tree crop agriculture.

Keywords: land use and land cover (LULC); multi-scale integration; artisanal small-scale mining (ASM); industrial mine transition; tree crop expansion

Introduction

Over the past few decades, a multitude of global and regional factors have shifted the land use and land cover (LULC) patterns surrounding Tortiya, Côte d'Ivoire from industrial mining to artisanal mining to tree crop based agribusiness. The political and economic effects of these changes have significant bearing on both current governmental decisions and on future land use planning for the region, but currently no record of LULC trends exists to inform decisions and policies. LULC throughout the region occurs at a wide range of geographic scales, from the extremely localized scale of artisanal small-scale mining (ASM) to the regional-scale of agricultural patterns. Furthermore, competing land requirements of mineral extraction and agribusiness sectors create the potential for renewed conflict in a country recently recovering from civil war partially incited by land ownership concerns. Remote sensing analysis provides independent quantification of land cover trends and is ideally suited for rural, data-scarce environments. However, the contrast of local- and regional-scales complicates typical remote

sensing LULC change methods. This study employs an approach for integrating multiple scales and sources of remote sensing data to quantify LULC trends over 46 years in the Tortiya area.

Background

Côte d'Ivoire is a key exporter of agricultural commodities such as cocoa, coffee, pineapples, and palm oil. Although Portuguese traders introduced Cashew trees to Africa in the 1500s, the growth of this crop as a key agricultural export was prompted by the formation of the African Cashew Alliance, sponsored by the United States Agency for International Development (USAID) in 2005. Since that time, it has become one of the country's principle exports, and was ranked as the world's second largest cashew producer in 2011 (Phipps 2011; ACI 2010, Foretell 2014). Since its introduction, large plantations of cashew trees have expanded across the country, particularly in the north where the climate is well-suited to cashew cultivation (ACI 2010; Foretell 2014).

Côte d'Ivoire's mineral sector includes industrial and artisanal extraction of diamonds, among other minerals. Both primary and secondary alluvial diamond deposits are present throughout the northern part of the country, including the Tortiya region. In the 1950's the Société Anonyme de Recherche et d'Exploitation Minières en Côte d'Ivoire (SAREMCI) mining corporation opened an industrial diamond mine along the Bou River in the Katiola Prefecture. The town of Tortiya was created by SAREMCI to house mine workers and provide associated services (Freudenberger 2015). The Tortiya diamond mine operated for nearly 30 years, producing between 150,000 and 175,000 carats (cts) per year at its height, until its abandonment in 1975 (Chirico and Malpeli, 2013). With the mine's closure, the town of Tortiya declined and conflict ensued between rival villages and former mine workers over ownership and usage of the land (Dejong 2013, Freudenberger et al. 2015). ASM began within the extent of the industrial mine soon after its closure. Though no official census of ASM activity was collected, ASM activity around Tortiya was estimated to diminish from around 40,000 artisanal miners in 1980 (UNGoE, 2011) to around 1,000 artisanal miners in 2011 (Chirico and Malpeli 2013).

Civil war in Côte d'Ivoire was sparked by issues of nationality and land ownership in the late 1990s, and led to a period of government instability and violence across the country in the early 2000s (Dejong 2013, Chirico & Malpeli 2013). Although violence was eventually quelled through international efforts, evidence that diamond sales contributed to financing of the rebellion resulted in an embargo on rough diamonds of Ivorian origin by the United Nations Security Council and the Kimberley Process (KP) in 2003. In spite of this embargo, ASM activity continued across the country, including in Tortiya (UNGoE 2011). Violence erupted again following presidential elections in 2010, but by 2014 efforts by Côte d'Ivoire's new government and international partners brought the country into compliance with KP regulations and legal diamond exports resumed.

Today, tensions over land ownership and usage in the Tortiya region are exacerbated by rapid LULC transitions from ASM and traditional agricultural activities to cashew tree crop plantations. In these situations those with mining interests and community land rights oppose the encroachment of cashew plantations and farmers (Freudenberger et al. 2015). Conversely, those who have invested in this new industry are concerned about the potential of mining activity disturbing valuable cashew orchards and harvests (Dejong 2013).

Remote Sensing of Artisanal Mining

Many remote sensing studies of LULC change in Africa have focused on a multitude of wide-reaching transitions from natural to agricultural and urban land covers, generally as the result of population and economic pressures or changing climate (Muriithi 2016, Dewan and Yamaguchi 2009, Kusimi 2008, Yiran, Kusimi and Kufogbe 2012, Wasige et al. 2013). Regional- and local-scale LULC changes are also of significant social and economic importance to community planning and conflict management endeavors, but may require more customized analysis techniques (Kibret, et al. 2016, Marx 2016). The temporal and spectral resolution of Landsat satellite imagery, along with its forty-two year archive (Landsat Missions, 2014) allows for analysis of decadal changes in regional-scale land cover patterns. However this scale of analysis, along with automated methods of classification may not be successful in detecting changes in other economically-significant but spatially compact land uses (Kibret, et al. 2016). Multiple studies have noted that the mapping of ASM locations using moderate-scale imagery such as that from the Landsat or SPOT sensors is difficult due to the small footprint of ASM and its spectral similarity with related land uses (Kusimi 2008, Elmes et al. 2014).

One of the first major efforts to map ASM over large areas utilized a variety of remote sensing methods, including automated classification of moderate resolution multispectral imagery, change detection using radar data, and aerial photography, as well as field methods. In this study, classification focused specifically on ASM-related land use and relied heavily on the spectral contrast between ASM land use and surrounding undisturbed dense vegetation (Telmer and Stapper 2007). Object-based image analysis (OBIA) classification methods have been investigated as a means of detecting the sedimentation of water-filled ASM pits and patterns of vegetation regrowth (Pagot et al. 2008), as well as a multi-scalar approach using 6.5 m and 0.5-1 m imagery to detect individual ASM features (Luethje et al. 2014) The latter method, though not field validated, also used a secondary textural analysis to differentiate between ‘potential mining areas’ from settlements. Sub-pixel classification methods, including spectral mixture analysis of Landsat imagery to detect sub-pixel changes in forest cover associated with ASM have also been investigated (Asner et al 2013; Elmes et al. 2014). At the other end of the spatial scale, the hydrological and geomorphological changes caused by industrial-scale mining operations have been

analyzed using moderate resolution DEM data combined with high-resolution satellite imagery (Emel et al. 2014, Merriam et al. 2015).

In each of these studies, large multi-pit ASM sites were successfully mapped, but potentially also included areas of mixed land use, such as settlements and transportation corridors. Moreover, much of the research on remotely sensed ASM mapping has focused on areas of relatively expansive ASM impact. Many of these studies report that small areas of ASM may have been omitted from the mapped areas. A second gap in the literature associated with remote sensing of ASM is the absence of a comprehensive, regional analysis of LULC changes associated with ASM. This study attempts to fill this gap by quantifying regional LULC and artisanal mining independently, then analyzing the two together in a multi-scalar analysis.

Study Area

Tortiya is located in the rural north central part of Cote d'Ivoire in the Niakaramandougou Department. The LULC study extent indicated by the red outline in figure 1, is based on the extent of the original SAREMCI mining concession. A smaller focus area, outlined in light gray in figure 1, was determined by the overlap of available high-resolution satellite imagery. The Tortiya region has an equatorial, winter dry climate (Kottek et al. 2006), which typically entails warm temperatures throughout the year and distinct wet and dry seasons. Precipitation in the region is concentrated between the months of May and October, when 75% of the yearly average 1,387 mm of rain occurs (Climatic Research Unit 2015). The warm, humid climate and seasonal rains promote quick regrowth of a woodland and grassland ecosystem (Sayre et al. 2014), and annual burning of this undergrowth is required to clear fields for traditional methods of agriculture.

The Tortiya study area is generally a low-relief terrain dominated by gently sloping interfluves capped by ferricretes (frequently termed *cuirasse* by French scientists) and bounded by reworked and eroded pediments of the ferricrete materials (*glacis*) (Peltre 1978, Teeuw 2002).The valleys contain alluvial materials in an alluvial flat or floodplain and terrace landforms (Chirico et al. 2013). The town of Tortiya itself lies on the banks of the Bou River approximately at the intersection of the Bou and one of its tributaries, Pekoua Creek.

Figure 1. The Tortiya study area, located in northern of Côte d'Ivoire.

Data

This study incorporates multiple sources of remotely sensed imagery and topographic data to assess the land cover changes that have occurred in the Tortiya region over the past 46 years. Both moderate- and fine-spatial resolution satellite imagery is used to assess LULC change, and terrain data are

acquired from global digital elevation models (DEMs) and regional topographic maps. The details of all data used in the analysis are described below and summarized in tables 1 and 2. Finally, field data collected in 2013 are used to validate LULC classification and to provide site-specific ASM details.

Satellite Imagery

The earliest remotely sensed imagery available for the region was collected by the Corona satellite on January 29, 1968. Project KH-4A (mission 1045-1) acquired panchromatic photography with a spatial resolution of up to 2 m depending on the latitude of the study area (McDonald, 1995). For this study, digital Corona image data was acquired from the USGS Earth Explorer web interface (http://earthexplorer.usgs.gov/) and subsequently resampled to 3 m resolution and georeferenced to reference imagery.

Cloud-free Landsat images were also acquired from the USGS Earth Explorer web interface (http://earthexplorer.usgs.gov/)for the dry-seasons of 1984, 1991, 2000, 2007, and 2014. These near-anniversary dates, on a roughly seven-year interval, capture long-term LULC changes and minimize annual and seasonal variations. Details regarding the specific date of collection, sensor, and scene identifier are shown in table 1. To reduce the effects of haze and smoke on the spectral signatures of land covers, each scene was atmospherically corrected to ground reflectance, then ortho-registered rectified to the 2014 image through cubic convolution resampling. Clouds along the western part of the 1991 image were masked using a two class unsupervised classification. Visible bands (bands 5, 4, and 3) of the 2014 Landsat 8 OLI image were pansharpened with the panchromatic band (band 8) of the same date to create a reference image.

An additional image data set used for this study was a NASA space photograph, collected by astronauts on the Space Shuttle on April 9, 1991,using a Hasselblad 250 mm camera on Kodak natural color positive Ektachrome, X Professional ASA-64, standard base film. The image was downloaded from the Earth Science and Remote Sensing Unit, NASA Johnson Space Center ‘Gateway to Astronaut Photography of Earth’ website (https://eol.jsc.nasa.gov/) as a geotiff, and georectified to the Landsat 8 pan sharpened image. It was used to assess accuracy of the 1991 Landsat LULC classification. High-resolution satellite images from the IKONOS and WorldView-1 sensors were used to assess the accuracy of the 2007 and 2014 classifications (respectively). These images, with additional images from the WorldView-1, GeoEye-1 and QuickBird1 sensors, were also used to perform local-scale LULC analysis.

Table 1: Remotely Sensed Imagery used in this study

Date	Satellite/ Sensor	Spatial Resolution (m)	Spectral Resolution (Number of bands)	Details (Scene ID, etc.)
Landsat Imagery				
1984 Nov 26	Landsat 5/ TM	30	Multispectral (7 bands)	LT51970541984315XXX07
1991 Jan 6	Landsat 4/ TM	30	Multispectral (7 bands)	LT41970541991006XXX03
2000 Jan 31	Landsat 7/ ETM+	30	Panchromatic & Multispectral (7 bands)	LE71970542000031AGS00
2007 Jan 7	Landsat 5/ TM	30	Multispectral (7 bands)	LT51970542007010MPS00
2014 Dec 31	Landsat 8/ OLI/TIRS	30	Panchromatic & Multispectral (8 bands)	LC81970542014365LGN00
Other Imagery				
1968 Jan 29	Corona	3 (resampled)	Panchromatic	Project KH-4A mission 1045-1
1991 Apr 9	Shuttle, Hasselblad 250mm camera	20	Kodak natural color positive film	NASA photo ID STS037-80-12 6° camera tilt; taken at 12:11 GMT
High-resolution Satellite Imagery				
2007 Dec 11	IKONOS-1	1	Panchromatic	11DEC07IK0101652po_372077
2008 May 5	WorldView-1	0.5	Panchromatic	WV120080505105727P02
2009 Dec 19	WorldView-1	0.5	Panchromatic	WV120091219111100P00
2010 Apr 6	GeoEye-1	1.6	Multispectral 4band	GE120100406105833M00
2011 Dec 25	WorldView-1	0.5	Panchromatic	WV120111225111246P00
2013 Dec 26	Quickbird	0.7 2.7	Panchromatic & Multispectral (4 band)	QB220131226100840P00 QB220131226100840M001
2014 Dec 13	WorldView-1	0.5	Panchromatic	WV120141213111949P

Field Observations

Field observation is an important part of studies of land use land cover change because it provides relevant local detail and understanding that cannot be obtained from remotely sensed data. In this study, field observations fell into two categories – one to provide both an in-depth understanding of artisanal mining practices, site characteristics and locations, and the second to allow for independent accuracy assessment of the 2014 land cover classification. Figure 2 shows the locations of each type of observation made during fieldwork. Additional details regarding each type of field observation are provided below.

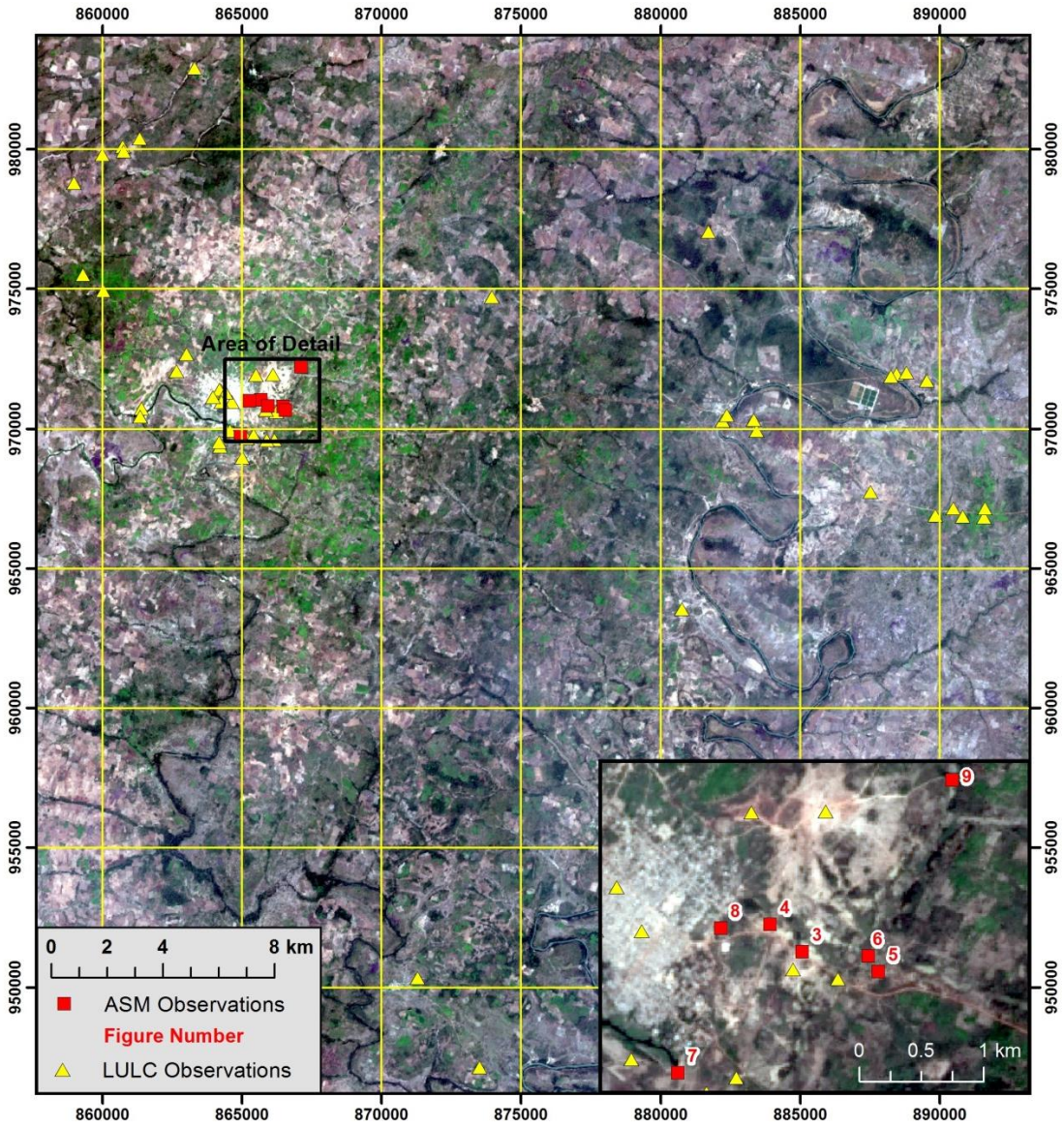

Figure 2. Locations of field observations. Visits made to observe ASM activity are shown in red, and the inset map shows the figure associated with these observations. LULC validation sites visited during 2014 are shown as yellow triangles.

2009 – 2013 ASM Observations

Field visits to areas of ASM activity near Tortiya were conducted during the dry seasons that occurred between 2009 and 2013. Several of these visits entailed aerial overflight observations in a helicopter, recorded primarily through low oblique photographs of the region and GPS. These observations improved understanding of ASM distribution throughout the immediate Tortiya region, provided detail about specific mining practices, and are also used as general validation of ASM activity interpreted from high-resolution satellite imagery.

From these field visits and overflights, it was observed that ASM has continued sporadically throughout the abandoned industrial mine area. Much of this mining targeted potentially diamondiferous gravels beneath the lateritic ferricrete. High levels of iron oxide in this semi-consolidated material make it appear mottled with white, orange-brown hues (Munsel colors 7.5YR 8/1, 10YR 8/4, 7.5YR 6/8), visible in the inset of figure 3.

At the sites visited, ASM pits varied in size, spatial extent, and depth depending on their location in the landscape and the duration of mining activity. Most pits were roughly 3-5 meters in diameter and one to several meters in depth. Figure 4 and 5 show two different aerial views of ASM sites with varying pit depths and spatial extents. It was observed that small, widely spaced exploration pits were used to determine the potential of a site. When and if diamonds were found at a site, ASM activity increased rapidly and pit diameter and depth increased.

Activity at ASM sites included both the digging for diamondiferous gravel material and the washing of this material to manually extract the diamonds. Figure 6 shows an ASM site where washing is the primary activity occurring. This activity adds substantial amounts of sediment to the water, resulting in high turbidity and a brighter spectral signature from the water. This is evident from figure 7, which shows an ASM site near the town of Tortiya where washing is the exclusive ASM activity. At this site, ASM miners take material from the old industrial mine spoil pile (figure 8 background) and re-wash it in the Bou River. At this site, it was observed that water turbidity alone was not indicative only of ASM activity. A multitude of other non-ASM activities, such as the laundering of clothing (also shown in figure 7 in the upper right corner) or disruption by livestock, also resulted in turbid water. Also evident from this figure is an example of the geomorphic changes caused by ASM activity. In this location, washing of gravel from the industrial spoil pile has increased the amount of sediment in this reach of the river, which over time has resulted in an artificial dam or barrage which has subsequently reduced the flow of the Bou and has increased flooding upstream. Although this change is small compared to the changes caused by the industrial mine, visible in the height of the spoil pile above the surrounding terrain (figure 8 background), the observed concentration of ASM activity in floodplains beyond the extent of the mine potentially influences the drainage patterns of the region during the rainy season.

ASM activity was also observed beyond the extent of the abandoned industrial mine. Located to the northeast of town in the Pekoua Creek floodplain, ASM activity shown in figure 9 was undertaken by groups of women searching for both gold and diamonds.

Figure 3. ASM activity targeting the gravel layer below the lateritic upper crust. Photo credit: Peter Chirico, USGS, February 2013.

Figure 4. Aerial observation of ASM activity within extent of abandoned industrial mine. Photo credit: Noora Jamsheer, UNGoE, March 2009.

Figure 5. Aerial observation of an ASM site in the floodplain to the east of the industrial mine. Photo credit: Simon Gilbert, UNGoE, February 2012.

Figure 6. ASM activity at this site entails primarily washing of gravel material. Photo credit: Simon Gilbert, UNGoE, February 2012.

Figure 7. ASM washing activity near the abandoned industrial mine spoil pile along Bou River channel. Photo credit: Simon Gilbert, UNGoE, February 2012.

Figure 8. Aerial view (facing west-southwest) of the abandoned industrial mine spoil pile and buildings. Photo credit: Simon Gilbert, UNGoE, February 2012.

Figure 9. ASM activity in ephemeral tributaries of the Bou River and Pekoua Creek occur almost exclusively in the floodplain. Photo credit: Peter Chirico, USGS, February 2013.

2014 LULC Observations

Multiple field visits were made to locations around the LULC study extent between August and September 2014 to collect land cover validation data. These observations allowed for an independent accuracy assessment of the 2014 LULC Classification. LULC was observed at 51 locations (figure 2, yellow triangles) distributed around the study area in a clustered sampling pattern, designed to minimize the high cost of travel in the area.

Methods

In order to assess both the small spatial-extent of ASM activity and other regional-scale land covers in the study area, LULC analysis is conducted independently at a regional scale and at a local scale. These two analyses are subsequently integrated together.

Regional-scale LULC Analysis

Six general land cover types (Table 2) were identified within the Tortiya study area for supervised classification. Training data were collected for each image date through visual interpretation of imagery and image derivatives, such as tasseled cap and the normalized difference vegetation index (NDVI). A support vector machine classifier with parameter optimization was selected for its ability to

differentiate between spectrally similar land cover classes with small training datasets (Jensen et al. 2009).

Table 2. LULC categories selected for the regional-scale analysis

LULC		Land Cover Description
1	Mining/ Bare	Closed industrial mine site or unpaved road
2	Forest (uncultivated)	Mature tree growth and dense woody shrubs, with partial-to-full canopy closure
3	Mixed vegetation	Vegetation growth other than uncultivated forest and Cashew tree crops, such as mixed grassland or herbaceous shrubs
4	Tree crop (cultivated)	Densely spaced cashew trees with partial-to-full canopy coverage
5	Urban	Mixed residential and commercial land use, indicated by the presence of pavement, compacted soil and/or buildings with highly reflective roofing materials
6	Water	Bodies of water and flooded grassland areas

Quantitative accuracy assessments were performed on the 1991, 2007, and 2014 classifications. For the 2014 classification, field data were used to perform an initial accuracy assessment. However the number of land cover observation sites visited in 2014 was limited by resources and access-constraints in the rough terrain, so accuracy was also assessed using other imagery. The 1991 accuracy assessment was performed using the NASA space photograph, and the 2007 accuracy assessment was performed using high-resolution satellite imagery. For each classification, accuracy was assessed at a set of stratified random points, with sample size based on multinomial distribution (Jensen 1995), and a confusion matrix was created to calculate producer's and user's accuracy. Since the aim of this part of the study was to quantify and map regional land cover in Tortiya, not to evaluate machine classification, misclassified Urban and Mining areas of the 1984 classification were manually corrected following the accuracy assessment. The area (in km^2) of each land cover as quantified by the classification was then calculated and the results were graphed to assess change over time.

To extend the analysis of economically significant land covers further back in time, Mining/ Bare and Urban land covers were manually interpreted from Corona imagery. These land covers were also digitized from the 1973 topographic map.

Local-scale analysis

Detailed land use associated with ASM activity was manually interpreted from each of the high-resolution images using the methods of Kauffmann et al. (2014). A point was digitized for each ASM pit interpreted from the high-resolution imagery, and attributed with the size of the pit (measured across the widest length of the pit). To minimize the subjectivity of manual interpretation, 2 image analysts independently interpreted ASM sites from each image, and only ASM sites consistently identified by both

analysts were kept. The average ASM pit size was calculated from all digitized pits from both 2007 and 2014.

ASM points from the 2007 and 2014 analyses were used to sample the corresponding Landsat classification to determine the effectiveness of moderate-scale analysis methods in analyzing ASM LULC.

Multi-scalar fusion of LULC analyses

In order to incorporate ASM land use into a regional-scale LULC analysis, interpreted ASM points were integrated with the Landsat LULC classification for 2007 and 2014. Based on field observations, although individual ASM pits in the Toritya region are typically small (3-5 m) in diameter, the space disturbed from walking paths, spoil piles, etc., might extend 15 m or more from the pit. For this reason the Landsat classification for each year was resampled to 15 m using nearest neighbor methods, and the 2007 and 2014 ASM point datasets were each converted to a 15 m raster aligned to the 15 m classification for that year. Pixels from the Mining/ Bare class from the ASM raster were inserted into the classification for the associated year. The area occupied by the Mining/ Bare class was assessed in both the original LULC classification and in the fused LULC classification to determine the effect of this method on the quantification of this land cover.

To evaluate the difference in spatial distribution of the Mining/ Bare class between the integrated classification and the original classification, a kernel density analysis was performed on the 15 m pixels classified as Mining/ Bare in each. In this analysis, the number of Mining/ Bare pixels within a 250 m radius was calculated, and output in units of Mining/ Bare pixels per km^2. The resultant raster was symbolized using a common geometric interval.

Results

Landsat SVM Classification results

The Landsat classifications are shown for the area of focus (figure 10), and achieved accuracies of 84.4%, 95.0%, and 87.6%/ 83.3% for 1991, 2007, and 2014 image assessment/ field assessment, respectively.

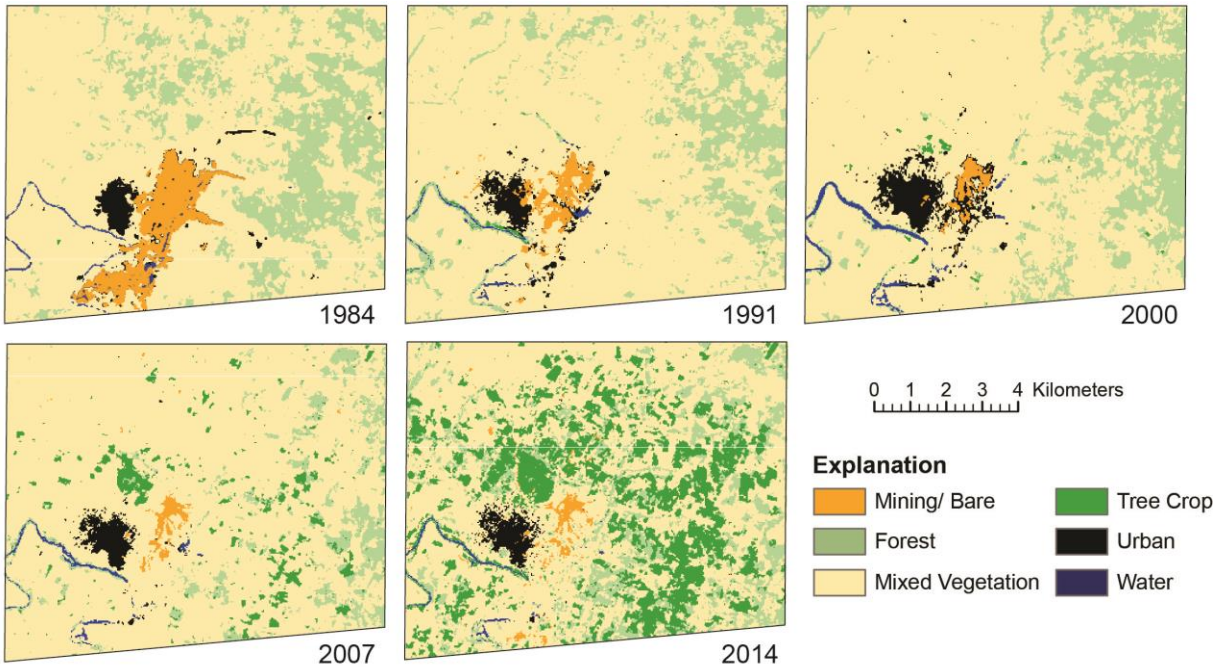

Figure 10. Landsat classification results within the focus area extent.

Producer's and user's accuracies for each class are shown in table 3. The classifications successfully differentiated spectrally similar land covers such as tree crops and forest (uncultivated), however there was some misclassification between the Mining/ Bare and Urban classes. This misclassification was visibly most severe in the 1984 image, and was manually corrected for the known extent of the abandoned industrial mine prior to analysis of land cover extent (as shown in figure 10). The percentage of each LULC calculated from the Landsat classifications, out of the total study area, is graphed in figure 11. Table 4 shows the LULC areas calculated from all data sources, including the Corona imagery, Topographic map, and LULC classifications. Figure 12 focuses on Mining/ Bare, Urban, and Tree Crop LULC for all dates of analysis. Each of these 3 LULCs is discussed in detail below.

Table 3. Accuracy assessment of SVM land cover classifications by year

	Classification Year – Overall Accuracy							
	1991 – 84.4%		**2007 – 95.0%**		**2014 (Image)– 87.6%**		**2014 (Field) – 83.3%**	
	Producer's	User's	Producer's	User's	Producer's	User's	Producer's	User's
Bare/mining	62	80	100	100	91	100	80	80
Forest	53	100	71	90	68	81	50	50
Mixed Veg	98	88	100	94	91	85	80	89
Tree Crop	100	10	83	100	91	91	88	88
Urban	80.	80.	83	100	100	100	100	67
Water	100.	73	100	100	91	100	100	100

Table 4. Area of each LULC class, calculated from the regional-scale land cover classifications, the interpreted Corona imagery and the topographic map.

	Area (km^2) of LULC Class						
	1968	**1978**	**1984**	**1991**	**2000**	**2007**	**2014**
Mining/ Bare	2.05	5.04	5.27	1.80	0.82	0.77	0.70
Forest	No Data	No Data	17.24	12.89	14.67	7.0	12.52
Mixed Vegetation	No Data	No Data	63.49	70.50	67.75	74.27	53.24
Tree Crop	No Data	No Data	0.02	0.21	0.40	3.58	19.75
Urban	0.46	0.45	1.35	1.83	3.20	1.48	1.25
Water	No Data	No Data	0.56	0.46	0.94	0.58	0.28

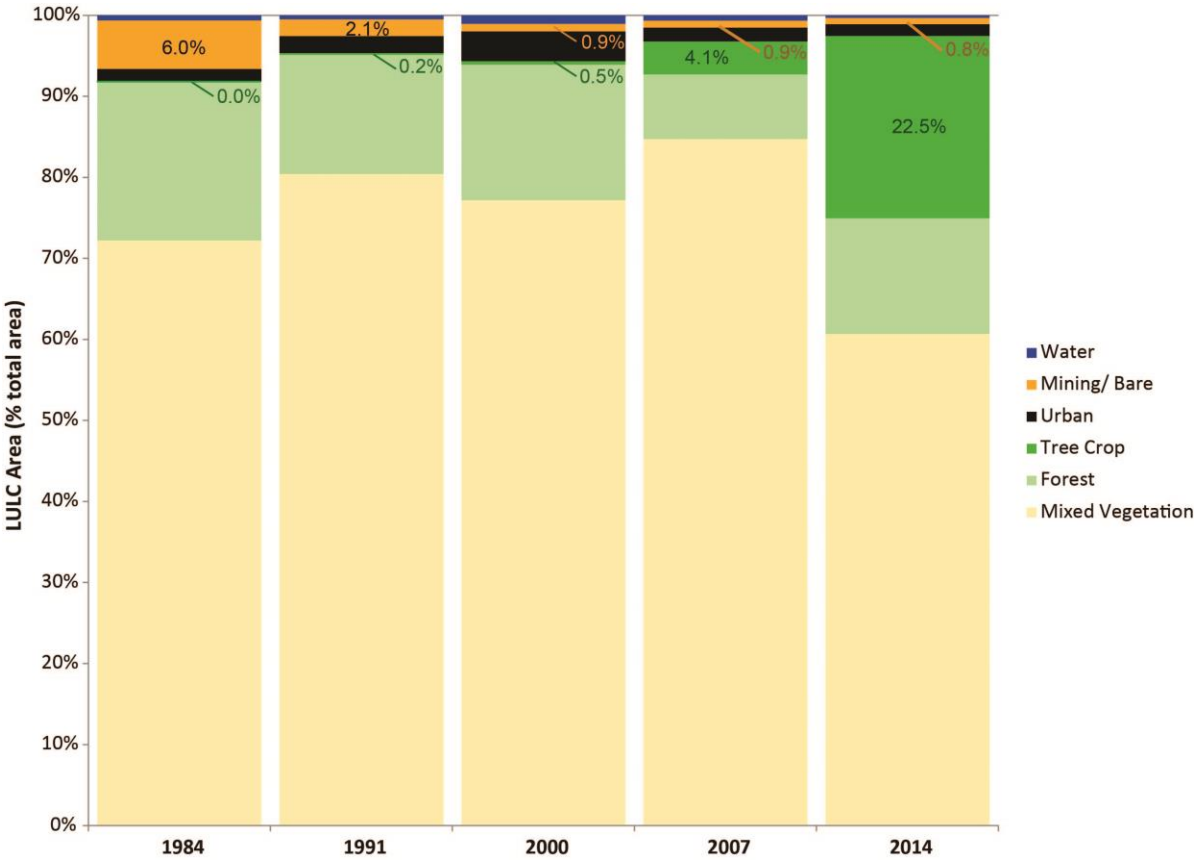

Figure 11. The 6 LULC classes are graphed as a percentage of the total area.

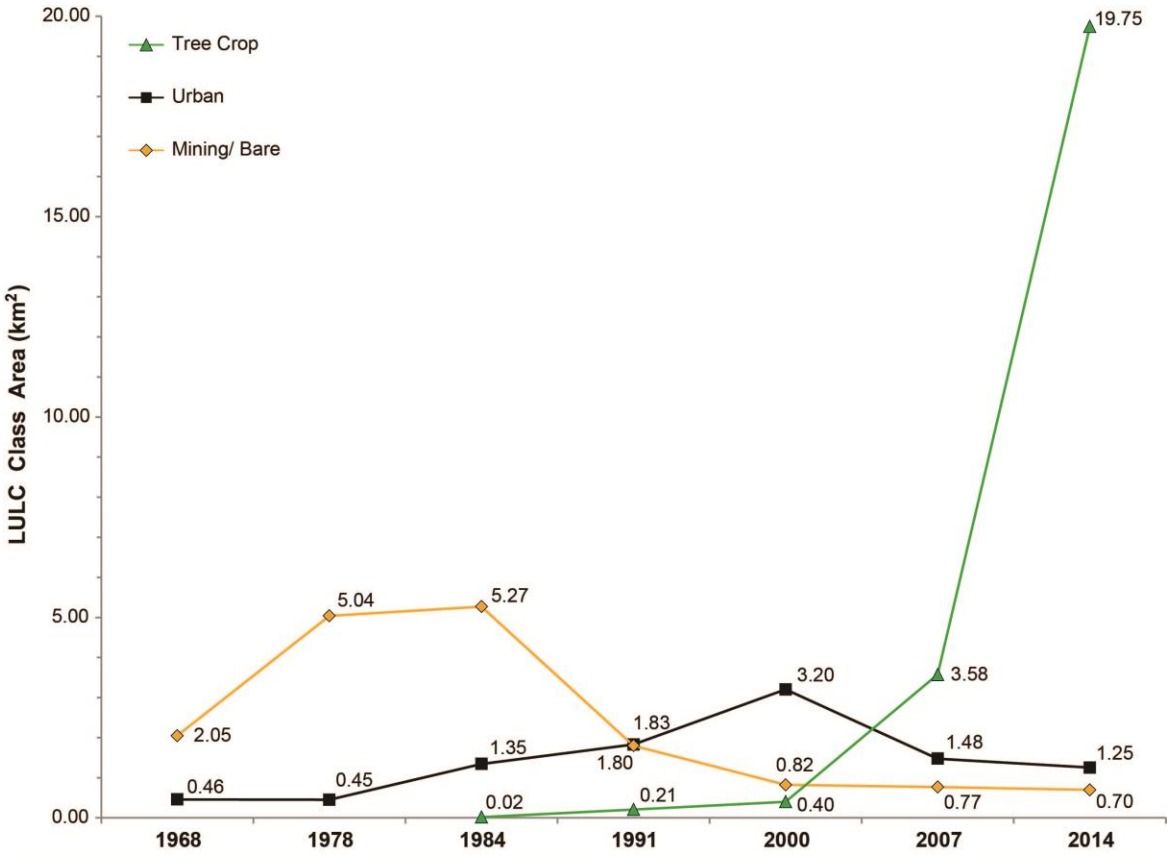

Figure 12. Area of Tree Crop, Urban, and Mining/ Bare land cover classes from multi-source analysis

The mine area increased greatly between 1968 (2.05 km^2) and 1978 (5.04 km^2), and continued to increase through 1984 (5.27 km^2). However by 1991 it had decreased substantially in extent (1.80 km^2), and this decrease continued through 2014 (0.70 km^2). Of importance is the spatial distribution of this class as captured by the LULC classifications (figure 10), which for all dates is principally within the extent of the abandoned industrial mine. The extent of Tortiya Urban area decreased between 1968 (0.46 km^2) and 1978 (0.45 km^2), before increasing to a maximum extent of 3.20 km^2 in 2000. Following this it steadily declined in area to 1.46 km^2 by 2014. The Tree Crop class first appeared in the classification results in 1984 (0.02 km^2). However large areas of this class did not appear until 2007 (0.21 km^2), and then it greatly expanded in 2014 (19.52 km^2).

Detailed ASM Changes

ASM pits interpreted 2007 and 2014 high-resolution satellite imagery are shown overlain on the LULC classification for the respective year (figure 13). Figure 14 shows a large-scale example of the

2007 interpreted points overlain on IKONOS-1 imagery. The average pit size measured in both 2007 and 2014 imagery was found to measure 3.7 m diagonally (2.6 m x 2.6 m), and to cover 6.76 m^2.

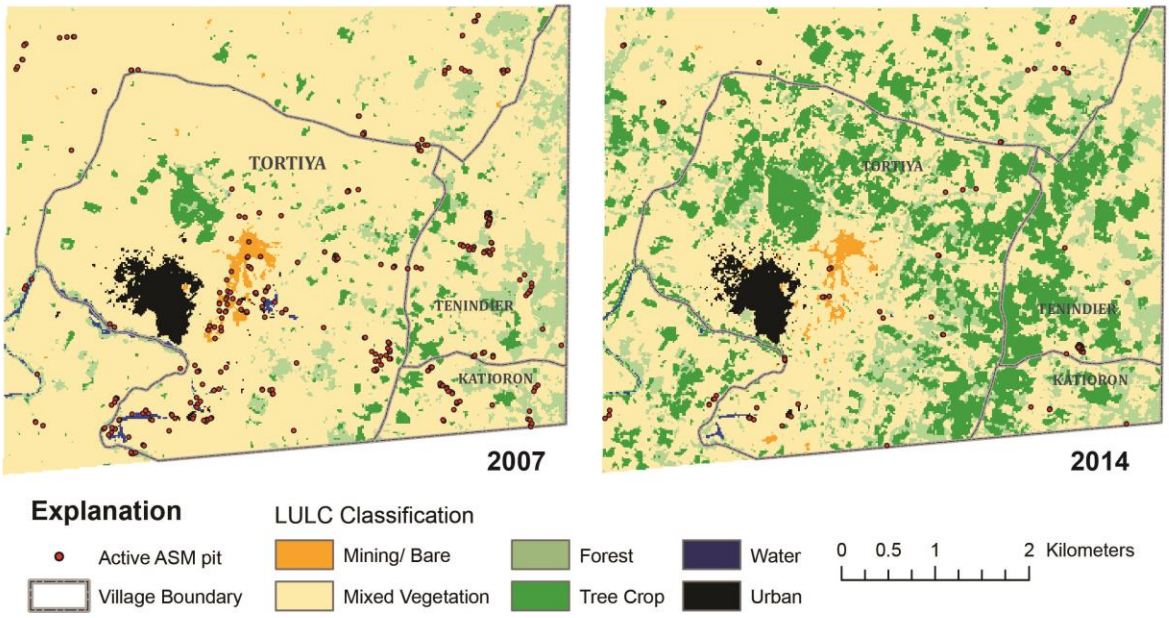

Figure 13. Interpreted ASM locations (red dot) were used to sample the LULC classification

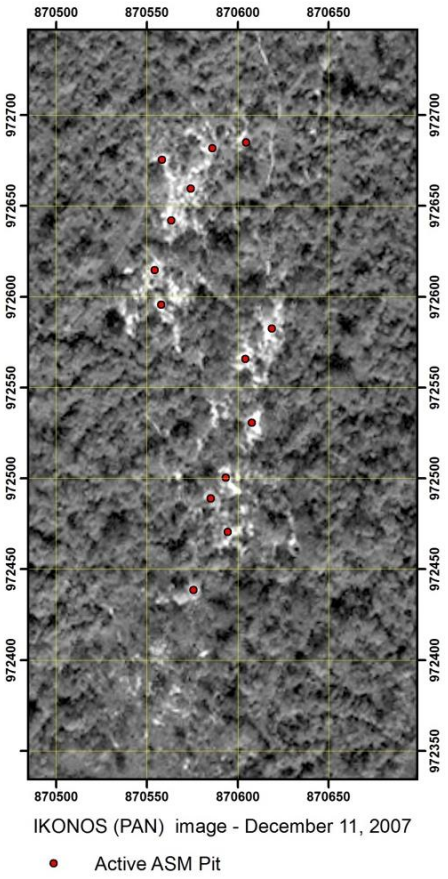

Figure 14. Example of ASM land use interpreted from high-resolution satellite imagery for 2007.

To determine the extent to which ASM activity is included in the Landsat multispectral classification of Mining/ Bare LULC, the 2007 and 2014 LULC classifications were compared to the ASM pit locations interpreted for 2007 and 2014.

The results of this sampling are shown (table 5) as a percentage of the total pits that fall within each of the six mapped LULCs. Although there were ASM pits that fell within the Mining/ bare LULC class in each year (6.9% in 2007 and 9.3% in 2014), the majority of ASM pits for both dates were located within the Mixed Vegetation class (86.2% and 75.9%, respectively). This suggests that support vector machine classification of Landsat does not successfully identify small areas of ASM in the Tortiya, Cote d'Ivoire landscape. This analysis also shows that little to zero ASM activity occurs within the area of the Tree Crop class in either 2007 (0.3%) or 2009 (0.0%).

Table 5. Percentage of ASM pits that fall within each LULC class, by year.

LULC Class	Percent ASM points (per year) located within each LULC Class 2007	2014
1. Mining/ Bare	6.9%	9.3%
2. Forest	2.2%	5.6%
3. Mixed Vegetation	86.2%	75.9%
4. Tree Crop	0.3%	0.0%
5. Urban	2.5%	9.3%
6. Water	1.6%	0.0%

Multi-scale results

The results of the integration of local-scale ASM analysis and the original (regional-scale) support vector machine classification are shown in figure 15. Table 6 shows the difference in spatial extent (km^2) of the Mining/ bare class in the integrated classification and in the original SVM classification for 2007 and 2014.

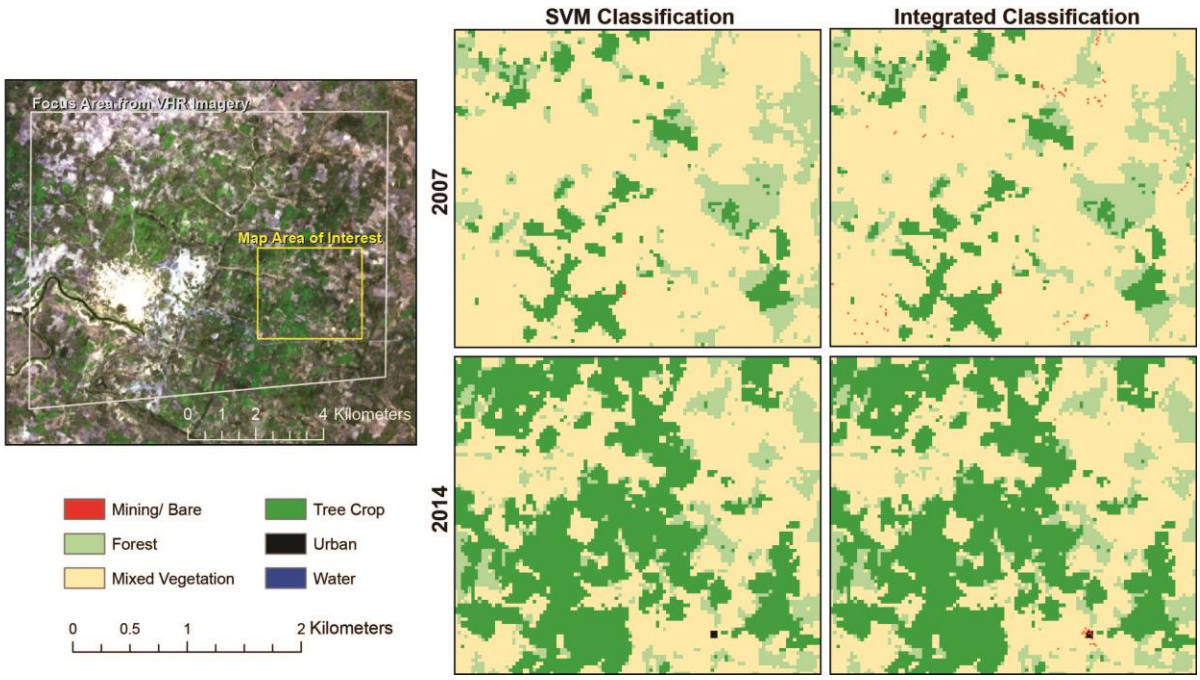

Figure 15. Comparison of SVM classification and integrated classification for 2007 and 2014.

Table 6. Area (km^2) of Mining/ bare class as calculated from the original support vector machine classification, from the Integrated classification, and the difference between these two values.

Year	Classification Area (km^2)	Integrated Classification Area (km^2)	Difference Area (km^2)
2007	0.77	0.83	0.06
2014	0.70	0.71	0.02

Although the difference in spatial extent between the SVM classification results and the Integrated Classification results is small, the spatial distribution of the Mining/ Bare class is substantially different for both years. The results of the kernel density (figure 16) analysis highlight this difference in spatial distribution.

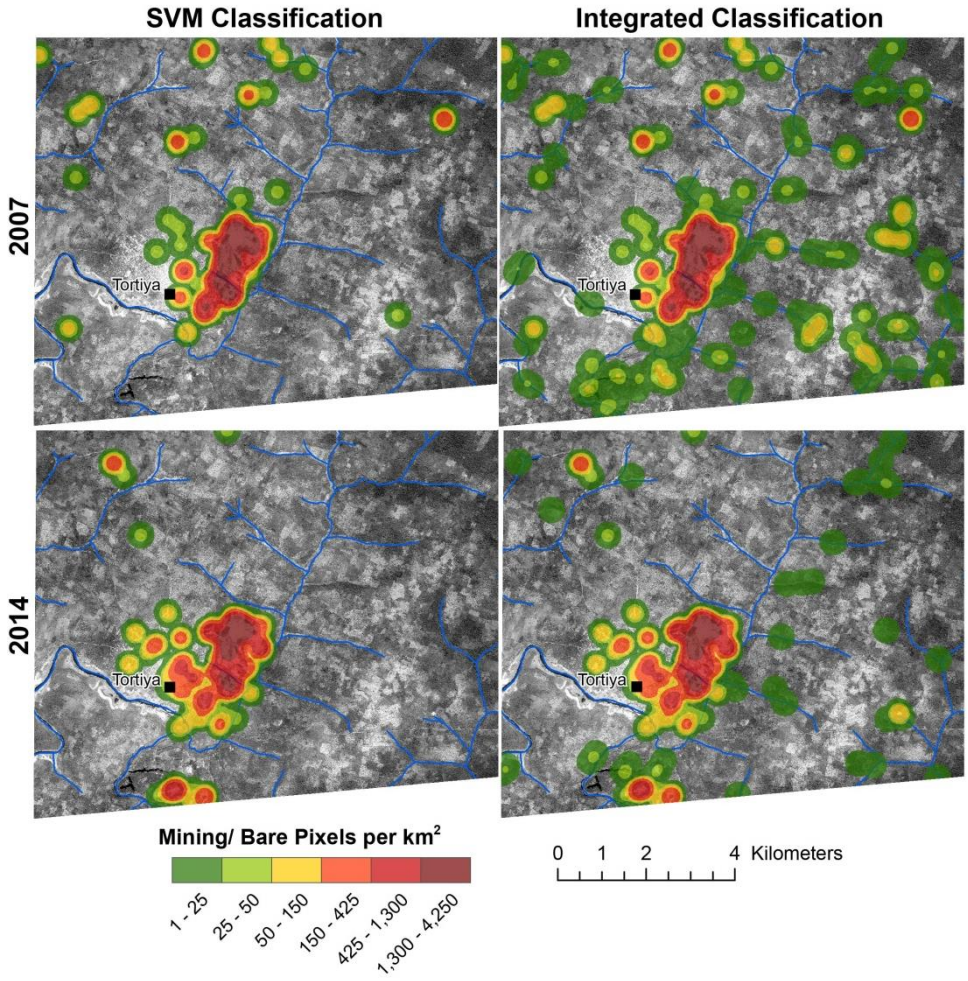

Figure 16. Kernel density analysis for each year in the original support vector machine classification and the integrated classification.

Discussion: Need for multi-scalar analysis

The 42 year archive of Landsat imagery and its consistent spatial and spectral resolution make it ideal for analysis of regional-scale LULC changes. In the Tortiya region of Côte d'Ivoire, the most notable of such changes is a large increase in the spatial extent of cashew tree crops. Automated SVM classification successfully captures this trend, as well as related decreases in Mixed Vegetation, which includes shifting agricultural land use, and in uncultivated Forest land cover. It also captures fluctuations in the extent of the Tortiya urban area. However this scale of analysis fails to capture fine-scale ASM land use as part of the Mining/ Bare land cover class.

When analyzed using high-resolution imagery, it is clear that ASM activity occurs throughout the Tortiya region in areas that are classified as Mixed Vegetation. This confirms earlier research and demonstrates that moderate-scale analysis based on Landsat classification is limited in its ability to quantify ASM activity in the mixed woody savannah landscape that surrounds Tortiya. This finding is not surprising when one considers the small average footprint size of ASM pits in this study (3.7 m diameter), compared to a 30 m Landsat pixel. The detection of fine-scale ASM activity within moderate-scale Landsat analysis is further hampered by the mixture of land covers that typically occurs within and surrounding an ASM site in this region. These land covers include dry and moist bare soil, turbid and clear standing water, and mixed herbaceous vegetation. Although high-resolution imagery is useful for identification of ASM activity, its limited temporal extent in this region and low spectral resolution makes it unsuitable for effective analysis of trends in other LULC classes, such as Tree Crops and Urban area. Thus characterization of comprehensive LULC classes and trends over time in the Tortiya area requires the integration of high-resolution and moderate-scale data and analysis.

Although the Mining/ Bare class in the integrated LULC classifications does not differ substantially in total area, the spatial distribution of this class varies substantially across the study area. The SVM classification shows Mining/Bare class is located almost exclusively in the area around the abandoned industrial mine whereas the integrated classification identifies pockets of mining that occur along many parts of the Bou River and its tributaries, including Pecoua Creek.

Artisanal mining occurs in diverse environments throughout the world, however much of the remote sensing literature regarding ASM has focused on mapping ASM extent within densely vegetated areas of the tropics. Not only does this body of research rely heavily upon the contrast of ASM activity with surrounding land cover (such as dense forest), it neglects to comprehensively assess changes in surrounding land covers that may be linked with ASM activity. The integration of fine-scale ASM interpretation with moderate-scale LULC classification allows for joint analysis of these different LULC scales in a way that meaningfully describes the spatial distribution of mining activity in this landscape. Furthermore, because the landscape-scale analysis of LULC is performed independently of the fine-scale

ASM analysis the method presented in this study could be used globally to evaluate any level of LULC detail.

Conclusion

Over the past 46 years, the primary economic driver of the town and surrounding area of Tortiya, Côte d'Ivoire has transitioned from industrial diamond mine to artisanal small-scale mining (ASM) to agribusiness in the form of cashew tree crops. More recently, the region also experienced substantial political and social changes due to civil war, which affected the entire country, but focused on the potential financial assets of diamondiferous areas in the northern part of the country, including Tortiya. In the post-conflict environment there remains the potential for land use conflict between those individuals of artisanal mining heritage and individuals of newer agribusiness focus. Collaboration between these two groups regarding LULC planning requires specific information regarding the history and geographic trends of each. This study has demonstrated a method of fusing together the fine-scale geographic distribution of artisanal mining with regional-scale LULC to provide a unified analysis of trends in the two. It showed that the amount of ASM activity occurring in the Tortiya area fluctuated significantly during the civil war and has diminished substantially in recent years. Conversely, the growth of cashew tree crop agribusiness in the Tortiya region has increased exponentially since 1984. It is likely that this growth will continue, potentially replacing artisanal diamond mining as the primary economic driver for the region.

References

African Cashew initiative (ACi). 2010. Analysis of the Cashew Sector Value Chain in Côte d'Ivoire. Deutsche Gesellschaft für Internationale Zusammenarbeit (GIZ) GmbH. Abidjan. p 76.

Asner, G., W. Llactayo, R. Tupayachi, and E. Ráez. 2013. "Elevated Rates of Gold Mining in the Amazon Revealed through High-Resolution Monitoring." Proceedings of the National Academy of Sciences 110 (46): 18454–59. doi:10.1073/pnas.1318271110.

Chirico, P., and K. Malpeli. 2013. "Reconnaissance Investigation of the Rough Diamond Resource Potential and Production Capacity of Côte d'Ivoire." U.S. Geological Survey Scientific Investigations Report 5185. 46p.

Climatic Research Unit. 2015. Precipitation data for Côte d'Ivoire, 1901-2013. University of East Anglia. Accessed online at: <https://crudata.uea.ac.uk/cru/data/precip/ > on 7/1/2015.

Dejong, T. 2013. “Diamond mining in Côte d’Ivoire: Programming options for the artisanal sector.” Report to the Diamond Development Initiative. ISBN 978-0-9809798-8-6.

Dewan, A., and Y. Yamaguchi. 2009. “Land Use and Land Cover Change in Greater Dhaka, Bangladesh: Using Remote Sensing to Promote Sustainable Urbanization.” Applied Geography 29: 390–401. doi:10.1016/j.apgeog.2008.12.005.

Elmes, A., J. Ipanaqué, J. Rogan, N. Cuba, and A. Bebbingon. 2014. “Mapping licit and illicit mining activity in the Madre de Dios region of Peru.” Remote Sensing Letters 5(10) :882-891.

Emel, J., J. Plisinski, and J. Rogan. 2014. “Monitoring Geomorphic and Hydrologic Change at Mine Sites Using Satellite Imagery: The Geita Gold Mine in Tanzania.” Applied Geography. 54: 243–49. doi:10.1016/j.apgeog.2014.07.009.

Foretell Business Solutions Private Limited. 2014. Cashew Handbook 2014: Global Perspective. 4th edition. India. p. 143. Accessed online at <http://www.cashewinfo.com/cashewhandbook2014.pdf> on 2016 SEPT 23.

Freudenberger, M., B. Tiam, C. Picard, S. Jiekak, and T. DeJong. 2015. “Property rights conundrums in artisanal and small-scale mining: Experiences from USAID projects in Côte d’IVoire, Guinea and the Democratic Republic of Congo.” Conference Paper. 2015 World Bank Conference on Land and Poverty. March 23-27. Washington, D.C., United States.

Jensen, J. et al. 2009. Image Classification, in: Warner, Tim A. et al. (Eds.), The SAGE Handbook of Remote Sensing, SAGE Publications Inc., California, pp. 269-281.

Kauffmann, M., I. Caravaggi, C. Louvrier, D. Al Khudhairy, P. Chirico, K. Malpeli, and J. DeWitt. 2014. Joint EU-US methodology for monitoring alluvial diamond mining activities in the Central African Republic: A European Commission (JRC) and United States Geological Survey (USGS) Report. JRC90218, 29 p.

Kibret, K., C. Marohn, and G. Cadisch. 2016. “Assessment of land use and land cover change in South Central Ethiopia during four decades based on integrated analysis of multi-temporal images and geospatial vector data.” Remote Sensing Applications: Society and Environment 3: 1-19.

Kottek, M., J. Grieser, C. Beck, B. Rudolf, and F. Rubel, 2006. “World Map of the Köppen-Geiger climate classification updated.” Meteorologische Zeitschrift 15(3): 259-263.

Kusimi, J. 2008. “Assessing Land Use and Land Cover Change in the Wassa West District of Ghana Using Remote Sensing.” GeoJournal 71: 249–59. doi:10.1007/s10708-008-9172-6.

Luethje, F., O. Kranz, and E. Schoepfer. 2014. “Geographic Object-Based Image Analysis Using Optical Satellite Imagery and GIS Data for the Detection of Mining Sites in the Democratic Republic of the Congo.” Remote Sensing 6(7): 6636–6661. doi:10.3390/rs6076636.

McDonald, R. 1995. “Corona: Success for Space Reconnaissance, a Look into the Cold War, and a Revolution for Intelligence.” Photogrammetric Engineering & Remote Sensing 61(6): 689-720.

Marx, A. 2016. “Detecting urban destruction in Syria: A Landsat-based approach.” Remote Sensing Applications: Society and Environment 4: 30-36.

Merriam, E., J. Petty, M. Strager, A. Maxwell, and P. Ziemkiewicz. 2015. “Landscape-Based Cumulative Effects Models for Predicting Stream Response to Mountaintop Mining in Multistressor Appalachian Watersheds.” Freshwater Science 34 (3): 1006–1019. doi:10.1086/681970.

Muriithi, F. 2016. “Land use and land cover (LULC) changes in semi-arid sub-watersheds of Laikipia and Athi River basins, Kenya, as influenced by expanding intensive commercial horticulture.” Remote Sensing Applications: Society and Environment 3 :73-88.

Peltre, P. 1977. Le ‘V Baulé : Héritage géomorphologique et paléoclimatique dans le tracé du contact forêt-savane.” Cahier Office de la Recherche Scientifique et Technique Outre-Mer (ORSTOM). 190, 193p.

Phipps, J. 2011. “Highlights of the Cashew Industry.” Red River Foods, Inc., Richmond: VA, USA. Accessed online at <http://www.africancashewalliance.com/sites/default/files/documents/2011CashewBroch.pdf> on 2015 DEC 14.

Sayre, R., J. Dangermond, C. Frye, R. Vaughan, P. Aniello, S. Bryer, D. Cribbs, D. Hopkins, et al. 2013. “A new map of Standardized Terrestrial Ecosystems of Africa.” African Geographical Review, Association of American Geographers. 24p.

Teeuw, R., 2002, “Regolith and diamond deposits around Tortiya, Ivory Coast, West Africa.” Catena 49: 111–127.

Telmer, K., and D. Stapper. 2007. “Evaluating and Monitoring Small Scale Gold Mining and Mercury Use: Building a Knowledge-Base with Satellite Imagery and Field Work.” UNIDO Project Final Report EG/GLO/01/G34. Victoria, BC.

United Nations Group of Experts. 2008. Report of the Group of Experts submitted in accordance with paragraph 10 of Security Council resolution 1782 (2007): New York, United Nations Security Council. 59p.

United Nations Group of Experts (UNGOE). 2011. Report of the Group of Experts on Côte d'Ivoire pursuant to paragraph 11 of Security Council resolution 1946 (2010): New York, United Nations Security Council. 80p.

Wasige, J., T. Groen, E. Smaling, and V. Jetten. 2013. "Monitoring basin-scale land cover changes in Kagera Basin of Lake Victoria using ancillary data and remote sensing." International Journal of Applied Earth Observation and Geoinformation. 21: 32-42.

Yiran, G., J. Kusimi, and S. Kufogbe. 2012. "A Synthesis of Remote Sensing and Local Knowledge Approaches in Land Degradation Assessment in the Bawku East District, Ghana." International Journal of Applied Earth Observation and Geoinformation. 14: 204–13. doi:10.1016/j.jag.2011.09.016.

Chapter 3 Comparison of DEMS derived from USGS DLG, SRTM, a statewide photogrammetry program, ASTER GDEM and lidar[1]

Jessica D. DeWitt, Timothy A. Warner, and Jamison F. Conley

Acknowledgements: The project described in this publication was supported in part by Grant/Cooperative Agreement Number G14AP00002 from the United States Geological Survey. The views and conclusions contained in this document are those of the authors and should not be interpreted as representing the opinions or policies of the U.S. Government. Mention of trade names or commercial products does not constitute their endorsement by the U.S. Government.

Abstract

Many digital elevation models (DEMs) now exist, enabling quantitative assessments of topographic change through DEM differencing. However, many of these DEMs are inherently different—they use different source data, as well as different preprocessing procedures and interpolation methods, and have different amounts of error which vary in different ways with topography. Understanding of these differences and errors is necessary prior to change detection analysis. This study evaluated available DEMs in the Mud 7.5' USGS topographic quadrangle in West Virginia, USA. We compare DEMs derived from the USGS digital line graphs (DLGs), the Shuttle Radar Topography Mission (SRTM), a statewide photogrammetric DEM, the ASTER GDEM v2, and a lidar DEM. Using the lidar data as a reference (RMSE 0.12 m), the USGS DLG and the SAMB showed low RMSE, while the SRTM and GDEM exhibited high RMSE and a systematic negative bias.

Introduction

A growing field of geomorphologic analyses relies on topographic change calculated from DEM differencing (James et al. 2012; Martínez-Casasnovas, Ramos and Poesen 2004; Wheaton et al. 2009; Blanchard, Rogan and Woodcock 2010). However digital elevation model (DEM) datasets differ widely in terms of their collection procedures, resolution, and accuracy levels (Bolstad and Stowe 1994; Gong et al. 2000). Grid-based DEMs are created through the interpolation of point or line based elevation values, which may be collected through in situ sampling, photogrammetry, or active remote sensors. Each data collection method has varying interaction with surface objects (most importantly vegetation) and incorporates varying levels of error in the resultant bare-earth DEM. These differences complicate direct comparison of one DEM to another DEM in change detection analysis and must be understood, and

[1] This manuscript has been published in GIScience & Remote Sensing (2015) vol 52 (2): 179-197.

preferably quantified, before topographic change can be calculated. This paper examines the differences between the major global and U.S. national freely available DEMs as well as a state-wide DEM through a case study in the Mud 7.5' Topographic Quadrangle, located in Boone, Lincoln and Logan Counties in southern West Virginia. Though other studies have focused on quantifying accuracy in one or two of the DEMs explored in this work, to our knowledge this study is the first to simultaneously compare the entire combination of the Advanced Spaceborne Thermal Emission and Reflection (ASTER) Global DEM (GDEM), the Shuttle Radar Topography Mission (SRTM), United States Geological Survey (USGS) 7.5" topographic digital line graph (DLG), and a statewide photogrammetric DEM in a single area of interest.

Widely available elevation datasets in the United States include USGS topographic maps and DLGs, published with varying dates (beginning in the early 1900s and updates continue through today), the SRTM DEM based on data acquired in 2000 (NASA Jet Propulsion Laboratory 2009), the National Elevation Dataset (NED) with varying publication dates (U.S. Geological Survey, available at http://earthexplorer.usgs.gov/), and the ASTER GDEM published in 2009 (NASA LPDAAC and METI 2011). Technological advances have improved the frequency of DEM creation and update, as well as the spatial resolution of the released models. However, the spatial extent of new elevation mapping campaigns is highly variable and many new DEMs are collected for small spatial extents, such as individual cities or counties. While these new DEMs are valuable improvements in data availability for their specific area of coverage, inconsistencies between these local scale DEMs and the 'best available' regional scale DEMs fragments and complicates topographic change studies conducted at the regional-scale.

Background

The following section reviews the procedures and methods for each of the different DEMs available in the WV study area to elucidate potential sources of elevation error and inaccuracy.

USGS DLG

One of the most widely available elevation datasets in the United States is produced by the USGS in the form of 1:24,000 scale contour-based topographic maps (also referred to as 7.5' topographic quadrangle maps). Contour maps were originally scribed manually from aerial imagery using stereoplotters. With the introduction of computer automation, photogrammetric methods are used to generate a set of mass points, breaklines and special points (Molander 2001). These elevation points are then interpolated to generate contour lines. Breaklines are used to modify the interpolated values in situations of abrupt elevation change (such as ridgelines, cliffs, or steep stream valleys). USGS 7.5' topographic printed maps were published on a quadrangle-by-quadrangle basis, beginning in the 1940s and officially completing in 1991 (Evans and Frye 2009, U.S. Geological Survey 2013). Since 1991, only

minor revisions have been made to printed products and the series has moved to a digital format (U.S. Geological Survey 2013). Since maps for each quadrangle are updated individually, neighbouring quadrangle maps frequently have different creation years (U.S. Geological Survey 2013).

USGS topographic map accuracy standards are based on the testing of points within the map space, and are worded to account for contour-based elevation models (U.S. Geological Survey 2006). In 7.5' quadrangle maps with a 20 foot contour interval, the accuracy standard translates roughly to a horizontal error of < 12.1 meter (m) and vertical error of < 3.05 m.

Contour maps imply a certain degree of smoothness of the underlying terrain and graphically convey a high degree of information to the informed reader, yet this implicit information does not readily transfer to digital and automated analyses. Because there are effectively no data between isolines, these areas are 'undersampled' on the map (Hengl and Evans 2009). While humans are able to read into and interpret meaning from the area between contours, they are effectively a void to computers because there is no metric for the distance between lines in the contour-to-grid interpolation algorithms. This is particularly problematic in areas of low relief, where these undersampled areas sometimes extend great distances from the nearest contour line (Hengl and Evans 2009). The interpolation applied to undersampled areas may poorly represent the true variation of the ground surface. Areas of high relief, where contour lines run closely together, are also problematic because poor scanning and manual digitization may introduce error to the interpolated surface. Despite these considerations, the amount of error introduced by digitization is generally negligible, and the DLG digitized contours generally maintain a similar accuracy to that of the original maps (U.S. Geological Survey 1993).

Unfortunately, the DLGs produced by the USGS do not carry quantified accuracy statements. Nevertheless, DLGs are useful in change detection, because unlike the conglomeration of elevation datasets in the more commonly used NED, DLGs carry a specific publication date—a key factor in change detection analysis applied to elevations. Once digitized, contour lines must be interpolated to a grid format to facilitate computerized spatial analysis. This process can also introduce error, which is complicated by the multitude of interpolation algorithms that exist. One popular algorithm is the ANUDEM program, which was developed to improve contour to grid interpolation by ensuring correct hydrologic drainage (Hutchinson 1988, 1989, 2006).

In summary, the DLG DEM's representation of the earth's surface is modified four times from the original photogrammetrically measured elevation values: once when the contours are drawn (which smoothes and generalizes topography across the earth's surface), once when 1:24,000 topographic contour maps are digitized (data modification in this step is generally regarded as minor), once when the digitized contour lines are interpolated to a grid (where original data values are potentially lost in favour of a new, modelled surface), and finally when the DEM values are modified to incorporate correct

hydrologic drainage (this last modification is, of course, potentially common to the preparation of all DEMs).

SRTM

In an 11-day mission in 2000, SRTM collected a global elevation dataset using -C and -X band interferometric synthetic aperture radar (IFSAR) (Hensley, Munjy, and Rosen 2007; NASA Jet Propulsion Laboratory 2009). Though data for the two bands was collected simultaneously, the coverage of the X-band is limited compared to the C-band and the processing into DEMs was done separately by the German Aerospace Center (DLR) and the National Aeronautics and Space Administration (NASA) Jet Propulsion Laboratory (JPL) (respectively). Some studies have found the X-band DEM to contain more outlier values and consequently to appear 'noisier' than the C-band DEM, and a direct comparison of the two DEMs revealed a systematic bias of higher error (around 10 m) in certain regions of the globe (Hoffmann and Walter 2006). SAR remote sensing has several advantages over photogrammetric methods of elevation data collection, including cloud penetration, potential night-time data collection, potential partial vegetation penetration, control over the angle of illumination, and the flexibility of different polarizations (Jensen 2007). Additionally, the SRTM 30° to 58° off-nadir swaths were collected from an altitude of 233 km yielding a wide swath width of 225 km (U.S. Geological Survey 2009). The DEM produced from the SRTM data has a spatial resolution of 1' (1 arc second or approximately 30 m, degraded to 3' outside the United States) and a vertical accuracy performance goal of ±16 m (Pierce et al. 2006). Global evaluations of vertical accuracy found the SRTM to have an average absolute height error of 9 m in North America (Rodriguez, Morris, and Belz 2006). However, in the mountainous, heavily forested region of Appalachia, this average error value may be higher (Bolstad and Stowe 1994; Blanchard, Rogan and Woodcock 2010). Comparisons to reference DEMs in West Virginia, Massachusetts, and New Hampshire found the SRTM represented a surface above the ground but not consistently at the canopy level (Hofton et al. 2006, Passini, Jacobsen, and Passini 2007). This inconsistent surface detection in areas of deciduous forest may be partially caused by the varying roughness of the vegetation canopy (Hensley, Munjy, and Rosen 2007). In mountainous regions, the SAR returns may also be affected by foreshortening, layover, and shadow, resulting in higher errors (Guth 2006).

ASTER GDEM

The ASTER sensor, located on board the Terra satellite, has both nadir and aft-looking near infrared bands. Together these bands produce a stereopair for every scene collected. The ASTER GDEM v1 was created photogrammetrically from a compilation of cloud-free ASTER stereopairs. Published in 2009, with a 30 m horizontal posting and a 20 m (95% confidence) stated accuracy, it was validated

globally by NASA at 25 m root mean squared error (RMSE) (NASA LP DAAC 2001, Chirico, Malpeli, and Trimble 2012). Other evaluations have found the GDEM to have an elevation RMSE between ±7 m and ±15 m (Abrams et al. 2010; Hirano, Welch, and Lang 2003). The GDEM includes a metadata raster that indicates the number of ASTER scenes used to calculate each pixel elevation. The inclusion of multiple imagery dates in the computation of each pixel's elevation value, while improving the overall accuracy, is one potential limitation of the GDEM for change detection studies. In topographically dynamic areas this pixel-to-pixel difference results in a widely varying elevation surface that cannot be tied to a specific point in time. Other studies have found two key sources of error in the first version of the GDEM—residual cloud artefacts and flaws in the stacking algorithm, used to calculate a single elevation value for each pixel from multiple image-pair DEMs (Chirico, Malpeli, and Trimble 2012; Hirano, Welch, and Lang 2003). An overall negative bias of the original ASTER GDEM has also been noted in multiple studies (Slater et al. 2011; Hirt, Filmer, and Featherstone 2010; Chirico, Malpeli, and Trimble 2012). A second version of the ASTER GDEM (v2) was released by NASA in 2011 and includes improved scene coverage, a smaller correlation kernel, and improved water masking. The accuracy of the GDEM v2 was found to be 17 m at the 95% confidence level when compared to absolute geodetic references over the Conterminous U.S. and in forested areas the DEM was found to be about 8 m above the 1' NED (ASTER GDEM Validation Team 2011).

Lidar

Topographic lidar is a relatively recent source of elevation data that relies upon precisely timed measurements of a laser registered spatially with a global positioning system (GPS) device and an inertial measurement unit (IMU). Distance from the sensor to the ground is calculated from the timed return of a near infrared laser beam. This distance value is converted to a ground elevation using the GPS/IMU measurements of the sensor's position in space (Fowler 2007). The accuracy of lidar elevation data depends on the degree of uncertainty in the position and orientation of the sensor and is potentially also affected by the sensor's field of view, scan rate, and acquisition altitude. Vertical errors are generally less than 0.3 m (Daniel and Tennant 2007). Portions of the NIR lidar pulse may penetrate vegetation through small holes in the canopy and through partial transmittance of the leaves (Rosette et al. 2012), thus potentially allowing the return of pulses from the ground. When paired with the high sampling density of lidar sensors, this vegetation penetration can result in highly accurate derived ground elevation values (Fowler 2007).

Having reviewed the various elevation data collection methods, the rest of this paper compares each of the above types of DEMs to a reference DEM for a specific site in the Appalachians of the USA.

Study Area

The Mud 7.5' topographic quadrangle (Figure 1) is used as a case study to evaluate topographic change detection and its associated challenges. This study area includes parts of Lincoln, Boone, and Logan counties, WV, USA, and exhibits evidence of the topographic changes caused by surface mining activity in the Hobet mine complex. Mining activity has increased in area across the northern part of the quadrangle from prior to 1975 to the present day. The southern part of the quadrangle is currently unaffected by mining.

Data and Pre-processing

Elevation data used in this study are listed in Table 1. The most recent (and assumed most accurate) elevation dataset available for the Mud Quadrangle is a lidar-based DEM collected in 2010. The SRTM DEM and the ASTER GDEM were downloaded from the USGS data browser Earth Explorer (http://earthexplorer.usgs.gov/). DLG data and the SAMB DEM were downloaded from the West Virginia GIS Technical Center (WV GISTC) (http://wvgis.wvu.edu).

DiCicco et al. (2011) performed an accuracy assessment of the lidar dataset by ground-surveying 321 points divided among four land cover categories across the southern WV coalfields area of interest. Of these 321 points, 98 lie within the boundaries of the Coal River watershed, which encompasses the Mud quadrangle. The accuracy assessment reported a consolidated RMSE of 0.118 m for the larger study area, and a RMSE of 0.209 m in the Coal River watershed. Since this error is substantially lower than the expected error in the other datasets, the lidar DEM (referred to hereafter as 'lidarDEM') is used as the reference topographic surface to which all other DEMs are compared to estimate their error.

Datasets were downloaded in the Universal Transverse Mercator projection of the North American Datum 1983 for zone 17 North (UTM NAD83 Z17N) or were transformed to this projection using cubic convolution. In order to prevent potential edge-artefacts, all datasets were obtained at a nine quadrangle extent surrounding the study area, converted to a DEM (as necessary), resampled to a 30 m grid by cubic convolution, and clipped to a 1 km buffer around the Mud quadrangle.

Other datasets used in this study include a boundary shapefile encompassing surface mining that was manually interpreted and digitized from 2011 National Agricultural Imaging Program (NAIP) imagery. NAIP imagery was obtained from the WV GISTC as a compressed county mosaic (http://wvgis.wvu.edu). This boundary was used to mask previously mined areas from the DEM comparison portion of the study. Finally, the 2006 National Land Cover Dataset (NLCD) was downloaded from the Multi-Resolution Land Characteristics Consortium (MRLC) and used to stratify sampling points by land cover (MRLC data are available at http://www.mrlc.gov/).

Methods

A difference raster was generated for each DEM by subtracting it from the lidarDEM (LidarDEM – each DEM). It was assumed that in mining areas differences between the lidarDEM and the other DEMs would be dominated by real change, so these areas were masked, and the resulting grids of the remaining non-masked areas were termed error rasters. Error rasters were assessed qualitatively and quantitatively. Slope was calculated from each DEM and was used to evaluate spatial non-stationarity and heteroskedacity in the error rasters.

Within the non-mined region of the quadrangle, a random sample of 1,000 points was generated and used to calculate error measures for each DEM. To locate points, the NLCD was clipped to the Mud quadrangle, and reclassified into the following classes: developed (high intensity, medium intensity and low intensity); forested (deciduous, coniferous and mixed); grassland (herbaceous and woody); and shrub/ crop/ wetland, which represent 4.1%, 72.2%, 17.5% and 0.2% of the land use for the study area respectively. The 1,000 points were allocated using a stratified random approach, with the number of points in each class being proportional to its area. Each DEM, slope raster, and error raster was sampled at the location of the points. These sample values were then used as the basis for the DEM evaluation and comparison.

The product of differencing each DEM from the lidarDEM is a new raster representing error in the DEM. In this raster, negative values indicate areas where the evaluated DEM surface lies above that of the reference DEM, while positive values indicate areas below that of the reference surface. To simplify visual comparison, these rasters were additionally processed to indicate the absolute value of elevation error. Quantitative assessment of the error in each DEM was performed in SAS JMP, and comprised descriptive statistical measures and distribution tests for both normal and non-normal distributions. The Shapiro-Wilk (W) test was used to evaluate the DEM value distributions, with the null hypothesis of a normal distribution. A t-test was used to test the degree to which the mean error value deviated from zero (Kanji 2006). Ordinary least squares (OLS) regression was used to evaluate the extent to which DEM errors could be explained by elevation and slope. Histogram plots were used to evaluate the variability of the error values, whether they were unimodal or multimodal, and whether they were predominantly positive or negative (Daniel and Tennant. 2007). Measures of central tendency, such as the mean and the median, provided insight into how the DEM compares to the reference DEM (whose mean and median are assumed to be close to zero) (Höhle and Höhle 2009). A t-test was used to determine whether the mean error value was significantly different from zero, where low values of the test indicate that the mean is not significantly different from zero (Rogerson 2006). The standard deviation of error values further elucidates the distribution of error values around the mean, where a high

standard deviation indicates the presence of many large errors in the DEM and/or systematic errors in the DEM (Höhle and Höhle 2009; Rogerson 2006).

The Shapiro-Wilk test was used to determine whether each DEM's error values are normally distributed. In this test, the null hypothesis is of normalcy; large p-values of the Shapiro-Wilk score result in rejection of the null hypothesis and indicate that the DEM error values are not normally distributed. Errors that are normally distributed are typically summarized using RMSE, where a low RMSE value indicates low overall error (Daniel and Tennant 2007). However, RMSE alone has been shown to insufficiently describe DEM error (Wechsler and Kroll 2006, Fisher and Tate 2006); therefore mean and standard deviation of the error were also calculated. Rasters that do not have a normal distribution of error values should be compared using non-normal error distribution measures, such as the median, normalized median absolute deviation (NMAD), and the 68.3% and 95% percentiles of the absolute error values. The NMAD provides a value for non-normal distributions that is conceptually similar to the standard deviation used to summarize a normal distribution (Höhle and Höhle 2009).

Results and Discussion

Figure 2 displays the absolute value error raster for each DEM, stretched on a consistent greyscale ramp, from a global minimum to global maximum (the minimum value of all error rasters and the maximum value of all error rasters). From this visualization it is apparent that the DLGDEM and SAMBDEM error rasters (Figure 2, A and D, respectively) have the lowest overall error values, and that the GDEM error raster has comparatively high values. For most DEMs error appears to be higher on moderate to steep slopes and lower in valleys, this is most apparent near the stream that runs through the southwestern end of the quadrangle in figure 2A-D.

Differences in each of the elevation data capture methods (photogrammetry, IFSAR, or lidar) result in differences in the detected elevation surface, and thus the derived DEMs are expected to differ. This is well documented by other studies (Bolstad and Stowe 1994; Kienzle 2004; Carlisle 2005; Fisher and Tate 2006; Li and Wong 2010) and the varying amounts of error found in the different DEM datasets in this study also supports this finding. Other research has found DEM error to be both non-stationary and heteroskedastic, and these two characteristics are qualitatively identifiable in all error rasters shown in figure 2. Additionally, DEM error has been found to be correlated with relief and slope (Bolstad and Stowe 1994; Carlisle 2005).

Table 2 displays OLS results for elevation and error, and for slope and error. These results support the qualitatively observed correlation between error and elevation and between error and slope. However, the impact of these two variables differs in magnitude and in the direction of error (whether positive or negative) for each DEM. For the DLGDEM, error is positively related to elevation (valleys

have low error, while peaks and ridges have higher error) and slope (steep slopes have higher error); in the case of elevation, this relationship is statistically significant. The SRTMDEM exhibits similar relationships, with both elevation and slope being significantly and positively associated with error. By comparison, the GDEM shows a significant relationship with slope, but this relationship is negative, suggesting that flatter slopes have higher error values. This relationship is likely an artefact of the local topography and land use —relatively flat areas are mostly confined to narrow valley bottoms, which are also the sites of most residential or industrial development in this area. Though there is relatively little area devoted to industrial and residential land use in the case study area, the potential exists for the GDEM to include building tops (effectively a digital surface model) in its representation of the bare earth. Other studies have found that high errors in the GDEM, though not limited to flat areas as seen in this study, are caused by the inclusion of multiple image dates in the photogrammetric DEM extraction. The use of multiple image dates maximizes cloud free areas in the imagery, however it also introduces errors in geometric alignment and mismatched pixels (Chirico, Malpeli and Trimble 2012). Overall, the very low R-squared values for all DEMs suggest that, though the relationships between error and elevation and between error and slope are significant, the two variables do not explain the majority of error found in any of the evaluated DEMs. At the very least, the mixed OLS regression results point to the complexity of the relationship between error and relief or slope and again highlight the differences between DEM datasets.

The histograms of the error values for each DEM provide an enhanced understanding of the amount and numeric distribution of error in each DEM (Höhle and Höhle 2009). Figure 3 shows DEM error raster histograms with uniform scaling to allow for direct comparison. The DEM error rasters exhibited markedly different histograms. The majority of the SRTMDEM and GDEM histogram values lie below zero, indicating that they model surfaces above the reference topographic surface. This observation is partially explained by their collection methods, which generally detect the upper surface of the forest canopy, and thus a surface that is not representative of a bare earth surface. Other studies have similarly observed the GDEM, both first and second versions, to have a negative bias on a global scale (Slater et al. 2011, Hirt, Filmer, and Featherstone 2010).

Descriptive statistics of the error values for each DEM are shown in table 3, and provide a quantitative comparison of the DEMs. A highly accurate DEM will exhibit a small minimum-maximum range, a normal unimodal distribution with a mean near zero, low skewness, a high p-value of the Shapiro-Wilk (W) test, a low RMSE, a low mean error, a low standard deviation, and a low t-score (Daniel and Tennant 2007). The following sections describe each DEM in terms of its errors, with the order of the DEMs discussed proceeding from lowest to highest overall DEM error.

The SAMBDEM had the lowest errors of all evaluated datasets within the study area. Its error value histogram exhibited the smallest range, with the mode centered near zero. However, the W test,

based on a null hypothesis of error values being normally distributed, was rejected at the 0.01% significance level ($p < 0.0001$). This demonstrates that the error value distribution is not normal, and thus non-normal tests were used to further assess the distribution of its values. A low standard deviation and a low t-score of 2.567, significant at the 5% level ($p < 0.05$), indicate that the majority of error values are close to the mean, which is significantly different from zero. The normalized median absolute deviation is lower for the SAMBDEM than for other DEMs. This, in conjunction with the comparatively low value of the 95% quartile measure, confirms that the SAMBDEM is the most accurate elevation dataset evaluated (excluding the lidarDEM, which was used as the reference dataset).

The DLGDEM also showed low error values within the study area. Its histogram exhibits a unimodal distribution with a small range and small standard deviation, centred near zero. These factors indicate low overall error in the DEM and few outliers. The W test for the DLGDEM, based on a null hypothesis of the error values being normally distributed, was not significant, which leads to an assumption of normality of the error value distribution. A highly significant t-score indicates that the sample mean is significantly different from zero, possibly indicating systematic bias in the error values. However, a comparatively low RMSE, low mean error, low NMAD value, and low 95% quartile support the conclusion of low errors overall in the dataset.

From the histogram, it is evident that error values in the SRTMDEM are generally much larger and have a wider spread around the mean than those of the SAMBDEM and DLGDEM. As noted above, the peak of this histogram is centred substantially below zero, the sample mean is significantly different than 0, and has a t-score of -49.957 ($p < 0.0001$). The W test, based on the null hypothesis of the error values being normally distributed, suggests that error values have a normal distribution. These factors indicate that the topographic surface of the SRTMDEM lies above the reference surface. This is not unusual in a DEM created from C-band IFSAR, which is impacted by dense vegetation and may not reach the ground (NASA Jet Propulsion Laboratory June 2009). The 12.59 m negative offset of the sample mean (indicating a modelled surface 12.59 m above the reference surface) is likely caused by the dense deciduous forest (of approximately the same height) that grows in the region (see Miliaresis and Delikaraoglou 2009 for a discussion on the effect of forest on the SRTMDEM). Despite the higher degree of error within the DEM and the vertical offset of the modelled topographic surface, the SRTMDEM is valuable for topographic change detection and analysis because it provides information not otherwise available during the 27-year time span between the collection dates of the DLGDEM and the SAMBDEM.

Error values associated with the GDEM were similar in range and magnitude to those associated with the SRTMDEM. Like the SRTMDEM, the GDEM histogram peaks well below zero and has a t-score which confirms that the mean is significantly different than zero. These two factors indicate that the

modelled topographic surface lies above the reference DEM surface. The W test, based on the null hypothesis of a normal distribution, was not rejected ($p < 0.59$). Despite its similarities to the SRTMDEM in magnitude and distribution of error values, the GDEM is fundamentally different than the other photogrammetric DEMs in its inclusion of multiple image dates for the elevation data extraction. This results in an inconsistent elevation surface in areas of dynamic topography and uncertainty regarding the specific associated date of the elevation at each pixel location.

Conclusion

Several regional-and global scale DEMs were compared to a high accuracy lidar DEM to quantitatively and qualitatively assess their differences in the rugged topography of the southern West Virginia coalfields. These DEMs included a grid interpolated from USGS 7.5' topographic map DLGs, the SRTM, a state-wide photogrammetric DEM (the SAMB), and the ASTER GDEM. Each DEM was compared to the lidarDEM by grid differencing and the resultant 'error' values were analyzed using various statistical measurements. In general these datasets form two groups: one of relatively high accuracy and another with relatively low accuracy. The high accuracy group comprises the SAMBDEM and the DLGDEM, with RMSE values of 3.05 m and 6.14 m respectively, and the low accuracy group the SRTMDEM and GDEM, with RMSE values of 14.90 m and 16.77 m, respectively. Though the RMSE value suggests a quick, global figure representing the accuracy of each DEM, a more comprehensive understanding of each DEM's representation of the topographic surface is gained through evaluation and comparison of other statistical values, such as basic descriptive statistics, histograms and tests for normalcy. OLS regression provides insight regarding the complex relationships between elevation, slope, and error. These values suggest that both the SRTMDEM and the GDEM describe a topographic surface substantially above that modelled by the lidarDEM. The GDEM suffers from a further problem for use in areas with rapidly changing elevations in that the modelled surface does not represent a single snapshot in time, but instead imagery acquired over an extended period. This problem may preclude the use of the GDEM in elevation change detection studies.

Future research will focus on methods to incorporate these measures of DEM inaccuracy into specific values to be added or subtracted from topographic change detection quantifications, as well as to methods that incorporate these uncertainties in topographic change products.

References

Abrams, M., B. Bailey, H. Tsu, and M. Hato. 2010. "The ASTER Global DEM." Photogrammetric Engineering and Remote Sensing 76 (4): 344-348.

ASTER GDEM Validation Team. 2011. “ASTER Global Digital Elevation Model Version 2 Summary Report.” Accessed 15 July 2014. https://lpdaacaster.cr.usgs.gov/GDEM/Summary_GDEM2_validation_report_final.pdf

Blanchard, S., J. Rogan, and D. Woodcock. 2010. “Geomorphic change analysis using ASTER and SRTM Digital Elevation Models in Central Massachusetts, USA.” GIScience & Remote Sensing 47 (1): 1-24.

Bolstad, P., and T. Stowe. 1994. “An evaluation of DEM accuracy: elevation, slope, and aspect.” Photogrammetric Engineering & Remote Sensing 60 (11): 1327-1332.

Carlisle, B. 2005. “Modelling the spatial distribution of DEM error.” Transactions in GIS 9 (4): 521-540.

Chirico, P., K. Malpeli, and S. Trimble. 2012. “Accuracy evaluation of an ASTER-Derived Global Digital Elevation Model (GDEM) Version 1 and Version 2 for two sites in Western Africa.” GIScience & Remote Sensing 49: 775-801.

Daniel, C., and K. Tennant. 2007. “DEM Quality Assessment, Digital Elevation Model Technologies and Applications.” Chapter 12 in: The DEM User’s Manual, edited by D.F. Maune, 395-440. Bethesda, MD: ASPRS.

DiCicco, S. 2011. “RAMPP WV Coal River QA/QC Report.” Memorandum. Accessed July 15 2014. http://www.wvview.org/data/lidar/SouthernWV/Metadata%20and%20Tiling%20Scheme/RAMPP_WV_Memo_20110722_Final.pdf

Evans, R., and H. Frye. 2009. History of the Topographic Branch (Division). U.S. Geological Survey Circular: Reston, Virginia.

Fisher, P., and N. Tate. 2006. “Causes and consequences of error in digital elevation models.” Progress in Physical Geography 30 (4): 467-489.

Fowler, R. 2007. “Topographic Lidar, Digital Elevation Model Technologies and Applications.” Chapter 7 in The DEM User’s Manual, edited by D.F. Maune, 207-236. Bethesda, MD: ASPRS.

Gómez, M., J. Lencinas, A. Siebert, and G. Díaz. 2012. “Accuracy assessment of ASTER and SRTM DEMs: a case study in Andean Patagonia.” GIScience & Remote Sensing 49 (1): 71-91.

Gong, J., Z. Li, Q. Zhu, H. Sui, Y. Zhou. 2000. “Effects of various factors on the accuracy of DEMs: An intensive experimental investigation.” Photogrammetric Engineering & Remote Sensing 66 (9): 1113-1117

Guth, P. 2006. “Geomorphometry from SRTM: Comparison to NED.” Photogrammetric Engineering and Remote Sensing 72 (3): 269-277.

Hoffmann, J., and D. Walter. 2006. “How Complementary are SRTM-X and –C Band Digital Elevation Models?” Photogrammetric Engineering & Remote Sensing 72 (3): 261-268.

Hengl, T., and I. Evans. 2009. “Mathematical and Digital Models of the Land Surface.” Chapter 2 in (Developments in Soil Science Volume 33) Geomorphometry: Concepts Software, Applications, edited by T. Hengl and H. I Reuter, 31-63. Amsterdam: Elsevier.

Hensley, S., R. Munjy, and P. Rosen. 2007. “Interferometric Synthetic Aperture Radar (IFSAR), Digital Elevation Model Technologies and Applications.” Chapter 6 in The DEM User’s Manual, edited by D.F. Maune, 142-206. Bethesda, MD: ASPRS.

Hirano, A., R. Welch, and H. Lang. 2003. “Mapping from ASTER stereo image data: DEM validation and accuracy assessment.” ISPRS Journal of Photogrammetry and Remote Sensing 57 (5-6): 356-370.

Hirt, C., M. Filmer, and W. Featherstone. 2010. “Comparison and validation of the recent freely available ASTER-GDEM ver1, SRTM ver4. 1 and GEODATA DEM-9S ver3 digital elevation models over Australia.” Australian Journal of Earth Sciences 57 (3): 337-347.

Hofton, M., R. Dubayah, J. Blair, and D. Rabine. 2006. “Validation of SRTM elevations over vegetated and non-vegetated terrain using medium footprint lidar.” Photogrammetric Engineering & Remote Sensing 72 (3): 279-285.

Höhle, J., and M. Höhle. 2009. “Accuracy assessment of digital elevation models by means of robust statistical methods.” ISPRS Journal of Photogrammetry and Remote Sensing 64 (4): 398-406.

Hutchinson, M. 1988. “Calculation of hydrologically sound digital elevation models.” In Proceedings of the Third International Symposium on Spatial Data Handling, Sydney Australia, August 17-19.

Hutchinson, M. 1989. “A new procedure for gridding elevation and stream line data with automatic removal of spurious pits.” Journal of Hydrology 106 (3): 211-232.

Hutchinson, M.F., 2006. ANUDEM Version 5.2 User Guide, Australian National University.

James, L., M. Hodgson, S. Ghoshal, and M. Latiolais. 2012. “Geomorphic change detection using historic maps and DEM differencing: The temporal dimension of geospatial analysis.” Geomorphology 37 (1): 181-198.

Jensen, J. 2007. Remote Sensing of the Environment. Upper Saddle River, NJ: Prentice Hall.

Kanji, G. 2006. 100 Statistical Tests, 3rd ed. Thousand Oaks, CA: Sage.

Kienzle, S. 2004. “The Effect of DEM Raster Resolution on First Order, Second Order and Compound Terrain Derivatives.” Transactions in GIS 8: 83-111.

Li, J., and D. Wong. 2010. “Effects of DEM sources on hydrologic applications.” Computers Environment and Urban Systems 34: 251-261.

Martínez-Casasnovas, J., M. Ramos, and J. Poesen. 2004. “Assessment of sidewall erosion in large guilles using multi-temporal DEMs and logistic regression analysis.” Geomorphology. 58: 304-321.

Miliaresis, G., and D. Delikaraoglou. 2009. “Effects of percent tree canopy density and DEM misregistration on SRTM/NED vegetation height estimates.” Remote Sensing 1: 36-49.

Molander, C. 2001. “Photogrammetry, Digital Elevation Model Technologies and Applications.” Chapter 5 in The DEM User’s Manual, edited by D.F. Maune, 121-141. Bethesda, MD: ASPRS.

Passini, R., K. Jacobsen, and R. Passini. 2007. “Accuracy analysis of SRTM height models.” In Proceedings of ASPRS Annual Conference, May 7-11, Tampa Florida. pp. 25-29.

Pierce, L., J. Kellndorf, W. Walker, and O. Barros. 2006. “Evaluation of the horizontal resolution of SRTM elevation data.” Photogrammetric Engineering & Remote Sensing 72 (11): 1235-1244.

Rodriguez, E., C. Morris, and J. Belz. 2006. “A Global Assessment of the SRTM Performance.” Photogrammetric Engineering & Remote Sensing 72 (3): 249-260.

Rogerson, P. 2006. Statistical Methods for Geography: A Student's Guide. 1st ed. Thousand Oaks, CA: SAGE Publications Ltd.

Rosette, J., J. Suárez, R. Nelson, S. Los, B. Cook, and P. North. 2012. “Lidar remote sensing for biomass assessment.” In Remote Sensing of Biomass - Principles and Applications, edited by L. Fatoyinbo, 3-26. Rijeka, Croatia: InTech.

Slater, J., B. Kroenung, W. Curtis, J. Haase, D. Hoegemann, C. Shockley, and K. Tracy. 2011. “Global assessment of the new ASTER global digital elevation model.” Photogrammetric Engineering and Remote Sensing 77 (4): 335-349.

U.S. Geological Survey, 1993. Data Users Guide 5: Digital Elevation Models, Reston, VA. Accessed 1 July 2014. http://pubs.usgs.gov/of/2003/0017/sus_met.txt

U.S. Geological Survey. 2006. “Map Accuracy Standards Fact Sheet FS-171-99.” http://pubs.usgs.gov/fs/1999/0171/report.pdf

U.S. Geological Survey. 2009. “SRTM Topography.” SRTM Documentation, 2.1. http://dds.cr.usgs.gov/srtm/version_1/Documentation/SRTM_Topo.pdf.

U.S. Geological Survey. 2013. USGS Topographic Maps. Online article. Accessed 1 May 1 2013. http://nationalmap.gov/.

Wechsler, S., and C. Kroll. 2006. “Quantifying DEM uncertainty and its effect on topographic parameters.” Photogrammetric Engineering and Remote Sensing 72 (9): 1081-1090.

Wheaton, J., J. Brasington, S. Darby, and D. Sear. 2009. “Accounting for uncertainty in DEMs from repeat topographic surveys: improved sediment budgets.” Earth Surface Processes and Landforms 35 (2):136-156.

Tables

Table 1. DEM datasets used in the local-scale topographic change detection study. Elevation datasets were acquired from the West Virginia GIS Technical Center (WV GIS TC), the National Aeronautics and Space Administration (NASA), and the Japanese Ministry of Economy, Trade, and Industry (METI).

Dataset	Date	Native Resolution	Creation Method	Source Agency
DLGDEM	1976	30 m	Aerial photogrammetry	WV GISTC
SRTMDEM	1999	30 m	C-band IFSAR	NASA
SAMBDEM	2003	3 m	Aerial photogrammetry	WV GISTC
GDEM	2009	30 m	Satellite photogrammetry	NASA/METI
LidarDEM	2010	3 m	Lidar	WV DEP

Table 2. OLS regression of elevation and DEM error, and slope and DEM error. There is a positive significant relationship between elevation and error in the DLGDEM and SRTMDEM. A significant relationship between slope and error exists in the SRTMDEM, SAMBDEM, and GDEM.

Variables	Metric	DLGDEM	SRTMDEM	SAMBDEM	GDEM
Elevation and error					
	R^2	0.048	0.020	0.003	0.001
	Prob > |t|	< 0.0001*	< 0.0001*	0.064	0.425
	Coefficient	0.024	0.021	0.003	0.005
Slope and error					
	R^2	0.002	0.038	0.005	0.009
	Prob > |t|	0.165	<0.0001*	0.034*	0.004*
	Coefficient	0.036	0.021	0.030	-0.146

ns $p > 0.05$, *$p \leq 0.05$, ** $p \leq 0.01$, *** $p \leq 0.001$, **** $p \leq 0.0001$

Table 3. Statistical measures of each error raster. Error rasters with a non-normal distribution are shown in grey fill, but all measures are calculated for all error rasters. While the majority of these statistical measures utilize the signed difference in elevation between the reference surface and the tested DEM surface (indicated by Δh), the non-normal error distribution measures of the 68.3 percentile and the 95th percentile evaluate the absolute value of the errors (indicated by $|\Delta h|$).

			SAMBDEM	**DLGDEM**	**SRTMDEM**	**GDEM**
Descriptive Statistic	Maximum	Δh	13.00	22.98	9.59	24.28
	Minimum	Δh	-20.96	-17.59	-36.17	-49.19
	$\underline{x}$	Δh	0.25	1.66	-12.59	-12.17
	Skewness	Δh	-0.123	0.136	0.016	-0.078
Test for normalcy	W-score		0.979^{****}	0.998^{ns}	0.998^{ns}	0.99^{ns}
	t-score		2.57^{**}	8.88^{****}	-49.96^{****}	-33.37^{****}
Normal Distribution Measure	RMSE (m)	Δh	3.05	6.14	14.90	16.77
	Mean error	Δh	0.25	1.69	-12.59	-12.17
	Σ	Δh	3.04	5.91	7.97	11.54
Non-Normal Error Distribution Measure	Median (50%)	Δh	0.14	1.44	-12.74	-12.14
	Normalized median absolute deviation	Δh	2.81	5.77	8.28	11.81
	68.3 %	$\lvert\Delta h\rvert$	2.81	6.08	16.49	17.86
	95 %	$\lvert\Delta h\rvert$	5.83	12.50	25.57	31.76

ns $p > 0.05$, $*p \leq 0.05$, $** p \leq 0.01$, $*** p \leq 0.001$, $**** p \leq 0.0001$

Figures

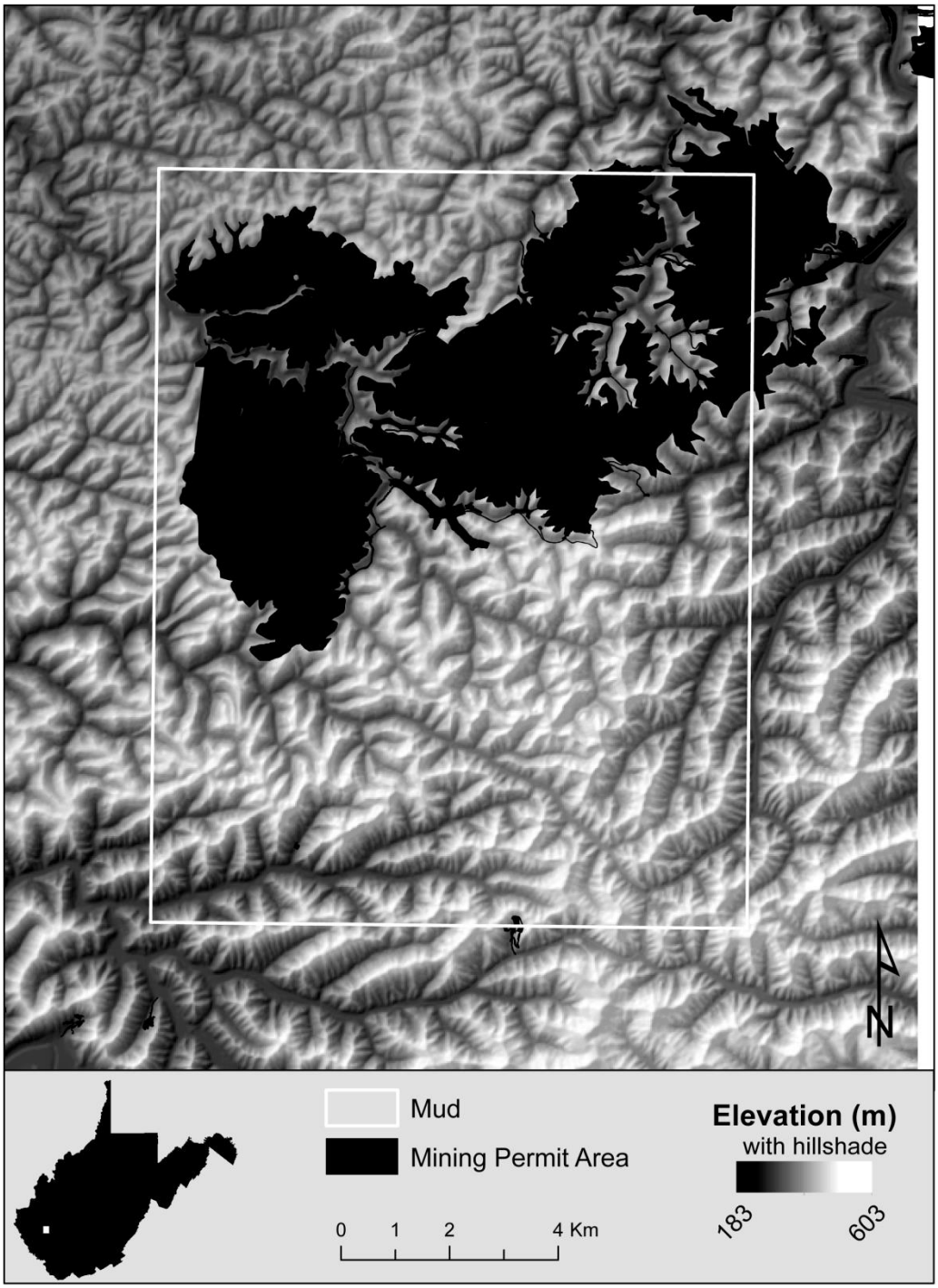

Figure 1. Study Area extent. The 'Mud' 7.5" topographic quadrangle in southern West Virginia. Areas that have a mining permit issued by the state, shown in black, are masked from the error analysis.

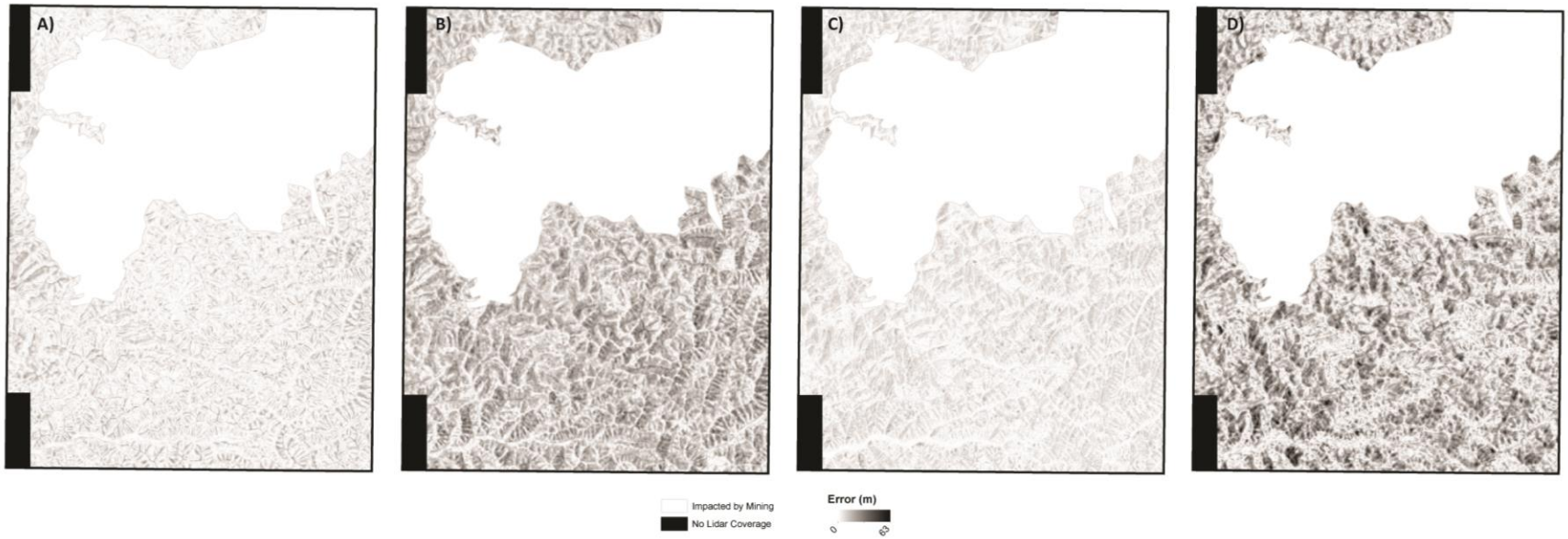

Figure 2. Error rasters generated from the lidarDEM - each DEM calculation. A) Lidar – DLGDEM; B) Lidar – SRTMDEM; C) Lidar – GDEM; D) Lidar – SAMBDEM. Areas of high error (large difference from the lidarDEM surface) are dark.

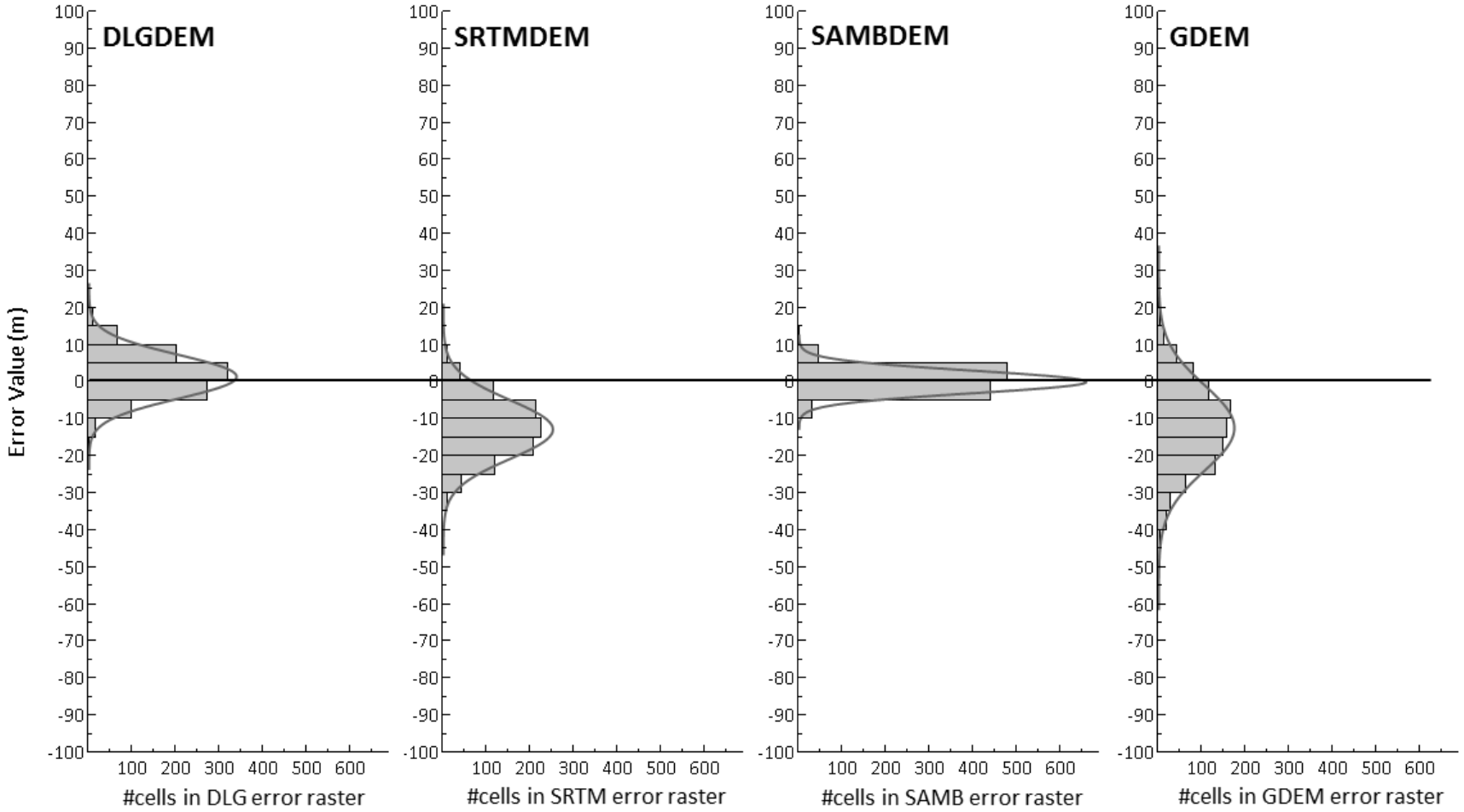

Figure 3. Error raster histograms for each DEM

Chapter 4 Creating high-resolution bare earth digital elevation models (DEMs) from stereo imagery using lidar point cloud procedures in an area of densely vegetated deciduous forest

Jessica D. DeWitt, Timothy A. Warner, Peter G. Chirico, Sarah E. Bergstresser

Abstract

For areas of the world that do not have access to lidar, fine-scale digital elevation models (DEMs) can be photogrammetrically created using globally-available high-spatial resolution stereo satellite imagery. The resultant DEM is best termed a digital surface model (DSM) because it includes heights of surface features. In densely vegetated conditions this inclusion can limit its usefulness in applications requiring a bare-earth DEM. This study explores the use of lidar point cloud filtering techniques, within the context of a case study of Prince William Forest Park (PWFP), Virginia, USA. The influences of land cover and leaf-on vs. leaf-off conditions are investigated, and the accuracy of the raw photogrammetric DSM extracted from leaf-on imagery was between that of a lidar bare-earth DEM and the Shuttle Radar Topography Mission (SRTM) DEM. Although the filtered leaf-on photogrammetric DEM retains some artifacts of the vegetation canopy and may not be useful for some applications, filtering procedures significantly improved the accuracy of the modeled terrain. The accuracy of the DSM extracted in leaf-off conditions was comparable in most areas to the lidar bare-earth DEM and filtering procedures resulted in accuracy comparable of that to the lidar DEM.

Introduction

Digital elevation models (DEMs) provide three dimensional (3D) information that can be vital for effective geospatial analysis (Wilson 2012; Tarolli 2014; DeWitt, Warner, and Conley 2015; Chirico, Malpeli, and Trimble 2012; Maxwell and Warner 2015; Maxwell, Warner, and Strager 2016). However, fine-scale, publically available DEMs have been generated for only limited areas of the world, placing a major constraint on the potential use of elevation information in remote sensing analysis. One way of addressing these data voids is by generating fine-scale photogrammetrically derived elevation data sets from commercial high-spatial resolution stereo satellite imagery. Though light detection and ranging (lidar) sensors have become the principle means of collecting highly accurate and precise elevation data, contracting lidar data for new areas can be expensive, and logistically impractical in remote areas of the world lacking air transportation infrastructure. Elevation data can potentially be generated from high-spatial resolution imagery at substantially less cost than lidar acquisition for almost any location in the world.

An elevation model derived from automated photogrammetric methods is best termed a digital surface model (DSM), because the derived elevations tend to include the heights of any objects that

obscure the ground. Removal of these surface features from the DSM, including trees and other vegetation, may be necessary for any geospatial application requiring a bare earth DEM. Thus, analysts considering the use of high-spatial resolution satellite imagery for generating their own DEMs are faced with multiple questions regarding what procedures to follow to try to reduce artifacts in the DSMs. In addition, for deciduous forests, the optimal season for image acquisition is not obvious. Leaf-on vegetation may obscure the ground surface, but leaf-off imagery may provide complex shadowing and branch patterns that may not necessarily be good for producing bare earth DEMs.

This study explores the use of commercially-available procedures designed for lidar data to filter vegetation and other surface features from a photogrammetrically derived DSM in forested environments with little or no built structures. Lidar-derived and photogrammetrically derived point clouds are compared to explore the potential of such tools in classifying and filtering elevation points belonging to surface vegetation from the DSM in an area of dense deciduous forest canopy. In order to assess the utility of such methods in areas of tropical vegetation and in leaf-on deciduous forest, both leaf-on and leaf-off photogrammetrically created DSMs are examined. Additional procedures utilizing only ancillary data gathered from the source imagery or photogrammetric DSM are explored, and the influence of land cover and vegetation canopy height on vertical accuracy of filtered DEMs is evaluated.

Background

Lidar is a comparatively new technology which uses precise distance calculation of laser pulse return time to estimate the elevation of a surface. Raw lidar data are normally represented by an unstructured point cloud of elevations of the ground surface and any overlying features. Classification of this point cloud into ground returns and surface features is performed by a variety of methods, selected by the specific characteristics of the area of interest (Meng, Currit, and Zhao 2010; Sithole and Vosselman 2004; Mongus and Žalik 2012; Ni et al. 2014; Passini, Betzner, and Jacobsen 2012; Montealegre, Lamelas, and De Riva 2015).

Photogrammetric methods calculate the Z (or elevation) dimension through measurement of parallax displacement in images taken from two different angles of view (Ni 2014). Traditionally photogrammetric DEMs were created for large areas at coarse scales using manual methods, or manually assisted computerized image matching. Recent advances in this field have automated image-matching algorithms (Sefercik et al. 2013) that transform the mathematical relationship between two-dimensional image space to 3D object space (Ni 2014, Toutin 2004). Furthermore, the introduction of epipolar geometry greatly improves computational efficiency and accuracy of pixel matching. The product of these procedures is a 3D dataset of matched-pixel locations in space from which a DEM can be interpolated (Ni 2014; Leberl et al. 2010; Toutin 2004). In bare and non-vegetated areas, these DSMs can be highly

accurate and therefore useful for detailed mapping of terrain (Sefercik et al. 2013, Müller et al. 2014; Bühler, Marty, and Ginzler 2012), however the presence of vegetation or man-made features complicates both visualization of terrain and extraction of hydrologic derivatives (Novoa et al. 2015). Furthermore, the vertical accuracy of fine resolution photogrammetric DSMs are not well-tested in areas of dense vegetation.

Study Area

An area of Prince William Forest Park (PWFP), in northern Virginia, USA, was selected (figure 1) for its location and data availability. The dense, closed-canopy deciduous and evergreen forest land cover of the region, coupled with its moderate topography was chosen to exemplify the strengths and weaknesses of photogrammetrically derived high-resolution DEMs and the filtering techniques explored in this study because they create an ideally challenging scenario for mapping ground elevations.

The geology of Prince William Forest Park largely reflects the tectonic processes that formed the Appalachian Mountain landscape, specifically tectonic compression during the Taconic, Acadian, and Alleghanian orogenies. In this landscape the late Precambrian to early Paleozoic metamorphic rocks, such as the Chopawamsic formation, are resistant to erosion, and outcrop along sharp ridgelines. Other rocks underlying the region include younger sandstone, shale, siltstone, carbonate rocks, and quartzite. Pyrite was mined extensively in the late 1800s to early 1900s. Acid mine drainage from the abandoned pyrite mine caused water quality issues in the Quantico Creek until reclamation efforts in the early 1990s. The western two thirds of the park is within the Piedmont physiographic region, and consists of complex rolling hills and steep-sloped valleys composed of unconsolidated colluvial deposits. The transitional zone between the Piedmont and the Atlantic Coastal Plain in the eastern part of the park is marked by a "Fall Line" of small waterfalls and rapids. To the east, the gentler topography of the Coastal Plain results in fluvial deposition landforms and wider valleys. The park is dissected by the Quantico creek and its tributaries (Thornberry-Ehrlich 2009).

Data

Data used in this study (Table 1), includes several types of satellite and aerial imagery, as well as multiple digital elevation datasets. High-resolution satellite imagery acquired from DigitalGlobe includes stereoscopic WorldView1, monoscopic WorldView3 (shown in Figure 1), and stereoscopic WorldView3. The 2015 imagery captures the leaf-on phase of vegetation canopy in the study area and the 2016 imagery captures the leaf-off phase of vegetation canopy. Aerial high-resolution orthoimagery collected during the spring of 2013 was used as reference for the PWFP site.

The reference DEM used in this study is the U.S. National Elevation Dataset (NED) 1/9 arc second (3 m) DEM. It was developed by the U.S. Geological Survey from lidar data collected by the

Federal Emergency Management Agency (FEMA) initiative to improve flood and emergency maps in northern Virginia. The lidar data were collected between April and October of 2011. The lidar dataset was independently tested (Dewberry 2012) to have a 5.5 cm vertical accuracy and a 1 m horizontal accuracy. The NED produced from lidar source data has an estimated RMSE of 0.87 m for the continental United States (Gesch, Oimoen, and Evans 2014). The NED was used for all direct elevation comparisons, and also to derive stream-lines. The raw lidar data is used in this study only for visual comparison between a true point cloud and a photogrammetric point "cloud."

The 1-Arc Second void-filled Shuttle Radar Topography Mission (SRTM) Version 3 DEM created from interferometric synthetic aperture radar (IFSAR) collected in 2009 and void-filled with ASTER GDEM2 data, is also used as a reference dataset. Originally this dataset was available outside the United States at 3-Arc Second resolution, however it was re-released in 2015 at 1-Arc Second resolution. Its global coverage makes it a common choice for elevation data if no higher resolution data are available.

Several ancillary datasets, including the PWFP boundary (shown figure 1), park map, and canopy height were acquired from the National Park Service. The canopy height dataset is derived from the 2010 lidar data at 1 m resolution and estimates vegetation canopy height above ground surface (Elmore, Guinn and Sanders 2013).

All datasets were clipped to the study area and projected to NAD 83 UTM 18 N. The re-projection of raster datasets was performed through cubic convolution resampling.

Methods

Software

In general, photogrammetry tasks were performed in PCI Geomatica, all tasks related to the classification or manipulation of the lidar point cloud were performed in GlobalMapper 17.1, and all other analyses were performed in ESRI's ArcGIS 10.1 (Table 2).

Land Cover Classification

The accuracy of both photogrammetric and IFSAR DEMs have been found to vary with landcover type (Fisher and Tate 2006; Hofton 2006), therefore a high-resolution land cover dataset was created from multispectral WorldView data to evaluate accuracy. Details regarding the creation and error evaluation of this dataset can be found in Appendix A, as they are not directly relevant to the focus of this study.

DSM Extraction

Digital surface models were extracted separately from both the leaf-off and leaf-on WorldView stereo imagery. To accomplish this, ground control points (GCPs) were manually selected to georeference

the stereo pair to reference imagery, image tie points were automatically identified, and block adjustment was performed. Epipolar pairs were extracted and then interpolated to create a grid-based digital surface model with 1.0 meter resolution.

The 2015 leaf-on imagery required two overlapping stereo image pairs (oriented one pair to the north of the second) to cover the study area. Eight GCPs were collected for each individual stereo pair, resulting in an overall RMSE of 0.5 m for the northern image pair and 0.9 m for the southern image pair. Mosaicking of the two extracted leaf-on DSMs was performed using an average operator and cubic convolution resampling. Only one stereo pair was required for the 2016 leaf-off imagery. Eight GCPs were collected with a RMSE of 1.16 m. Finally, all DSMs were converted to LASer (LAS) point cloud file format, where each point represents the elevation value at the center of the grid cell.

Filtering surface features from the DSM

Multiple lidar processing workflows were investigated to filter surface features from the photogrammetric DSMs to create a bare earth DEM. A variety of procedures are described in the following sections, but all entail an initial classification of outlier values as noise, then the remaining non-noise points are classified as ground or non-ground. Additional procedures using vegetation point classification and ancillary data are explored. An overview of the specific procedures used in each workflow is given in Table 3.

Classification of Outlier and Ground points

The first step in point classification is the labeling of elevations greater or less than two standard deviations from the local mean, and outside of the global range of 0 – 135 m (established using the limits of the SRTM elevation range in the study area) as noise. Of the remaining points, ground points were classified as those points with a relatively small curvature and small vertical difference from the average of the local area. These parameters were optimized iteratively through comparison of each ground point's elevation to the NED. The difference value and subsequent calculation of mean error from the collective difference values of all points was used to characterize the success of parameter settings. From this analysis a local window (set to 10 m) was used to determine a minimum vertical departure (set to 1.5 m) for the photogrammetric DSMs, and 4 m and 0.6 m (respectively) for the raw lidar data. Additional parameters of maximum height delta and maximum expected terrain slope were set to 35 and 9, respectively, but had comparatively little influence on the classification.

Additional Procedures Tested

Additional procedures were explored as potential methods for reducing elevation inaccuracies and to improve the correctness of hydrologic flow across the filtered DSM. These additional procedures included a vegetation offset and geomorphic correction method.

Vegetation offset

Inaccuracy in the filtered photogrammetric DSMs results partially from interpolation across large areas classified as 'non-ground.' Unlike multiple-return lidar data, which generally does not have such large gaps because a few returns reach the ground surface even in dense closed canopy forest, these 'non-ground' points in the photogrammetric point cloud are gaps in the ground surface and must be filled through interpolation of surrounding ground points. Thus a procedure to utilize vegetation points through a vertical offset was investigated. A point was classified as vegetation if the plane between it and the nearest two ground points exceeded a certain slope. This 'planarity'-based evaluation was performed for a local window throughout the study area. The elevation of points classified as 'vegetation' was then reduced by 10 m, based on the average canopy height observation from Elmore, Guinn and Sanders (2013).

Geomorphic correction by proximity to stream

Consideration was also given to hydrologic modeling of water flow across the DSM, which requires well-defined drainage pathways. To improve flow, key drainage pathways were defined and improved through a vertical offset. The orthorectified 2015 monoscopic imagery was used for the manual identification and digitization of stream paths as line features. Each identified stream is at least 5 m wide and is an important drainage element contributing to the geomorphology of the study area. Digitized streams were therefore buffered by 5 m on each side of the stream, and all ground points within the buffered area were given a 10 m negative vertical offset to improve the flow of water across the filtered DEM.

Comparing lidar and photogrammetric point clouds

Lidar and photogrammetric point clouds were compared by quantifying the area of the gap between each set of three points, after a triangulated irregular network (TIN) was applied to the point clouds. These gap areas are important because they represent the space that must be interpolated to create the raster DEM. The point clouds were also qualitatively compared through visualization of profiles through the point clouds.

Bare Earth DEM generation and error evaluation

Once filtered for surface features, each point dataset was interpolated to a raster DEM by first creating a triangular irregular network (TIN) of points, thinned using a local-mean 5 m window.

The accuracy of these bare earth DEMs was assessed through point-sample comparison to the reference DEM. A dataset of 1,000 random points, stratified by the land cover class, was generated. Table 4 describes the proportion and number of points allocated for each of the three land cover classes. At each point, the elevation of each filtered DEM was extracted and error was calculated as the difference between the filtered DEM and the reference DEM (filtered DEM minus reference).

Several studies have discussed the inadequacy of global error estimates, such as the root mean squared error (RMSE) and mean error, in summarizing the accuracy of a DEM (Höhle and Höhle 2009; DeWitt, Warner, and Conley 2015), and suggest additional statistical metrics to provide a complete evaluation of error irrespective of data distribution. Therefore, in addition to the normal distribution metrics of mean, standard deviation, and RMSE, non-normal distribution metrics of the Wilcoxon median interval, 68.3% quantile, 95% quantile, and normalized median absolute deviation were calculated.

To test whether the filtering methods reduced error in the photogrammetric DSM, the one sample Wilcoxon statistic was used. A one-tailed null hypothesis tested whether the filtered DEM median values were less than the corresponding DSM median. The null hypothesis for this test states that the median values of the filtered DEMs are not significantly ($\alpha < 0.05$) lower than that of the DSM. Similarly, a follow-up Wilcoxon test evaluated whether WV1_FIL2 and WV1_FIL3 had lower median error values than that of the simple ground filtered DEM (WV1_FIL), with a null hypothesis states that the median values of WV1_FIL2 and WV1_FIL3 are not significantly ($\alpha < 0.05$) less than the median of WV1_FIL.

The impact of land cover on DEM error was evaluated through the analysis of error values within each land cover category. For example, only error values of the 53 points falling within open areas are used in the calculation of error metrics for the Open land cover category, etc. Correlation between the canopy height raster and the error raster for each filtered DEM is used to evaluate the influence of vegetation height on error.

Results

Comparison of lidar and DSM point clouds

The density of a photogrammetric point cloud depends on the resolution of the stereo imagery, but is typically 4 points/m^2 for 25 cm imagery. Although this is similar to that of lidar, the lidar and photogrammetric point clouds have inherently different 3D structure. The lidar point cloud's multiple-return structure captures both the ground elevation and the vegetation canopy, resulting in multiple elevation (Z) values for each X,Y location in space. By comparison, the photogrammetric point cloud

contains elevation values for only the reflective surface of the imaged area. The resulting point cloud captures either ground or vegetation elevations, resulting in large gaps in ground elevation measurement. Figure 2 compares a cross-section of the lidar point cloud (A) to that of the leaf-on photogrammetric point cloud (B). From figure 2 it is clear that, while there are few areas of a lidar point cloud that lack coverage in ground points, the photogrammetric point cloud may have large areas that do not contain a single ground point. The removal of non-ground elevation values from a photogrammetric point dataset results in a loss of the elevation measurement for the area of those points, and necessitates interpolation of elevation from surrounding points.

This is quantitatively evident in comparison of the triangle facet areas of the TINs created from the ground returns of each dataset, shown in Table 5. The larger average area of TIN facets in the photogrammetric DEM compared to those of the lidar DEM (2.3 m2 and 0.2 m2, respectively) indicates that it has sparser ground measurement and more interpolation.

Figure 2 also demonstrates that there may be a vertical discrepancy between the elevations of photogrammetric ground points and elevations of lidar ground points. This is because the points may capture low areas in the vegetation canopy instead of the ground, and still fulfill the local height and planarity classification parameters for ground points in the photogrammetric point cloud.

Interpolated digital terrain models

All DEMs are shown planimetrically in figure 3 using the same color ramp and linear 0 – 125 m stretch to allow for direct visual comparison of the reference DEM (figure 3A) and SRTM (figure 3B) to the photogrammetrically derived raw DSMs (figure 3C and 3G) and filtered DSMs (figure 3D-F, 3H). Visualization of the DEMs in profile is useful in evaluating the degree to which each approximates the ground surface of the reference DEM. To enable this 3D comparison, figure 4 shows the profile of each DEM along a transect. Table 6 displays the results of the error assessment using descriptive statistics, normal distribution accuracy metrics and non-normal distribution accuracy metrics. All photogrammetric DEMs, except the WV3_DSM were found to have negative error skew, indicating that the modeled elevation surface lies below the reference surface. The presence of skewness suggests a non-normal error distribution and indicates that non-normal distribution metrics, such as the 68.3 percentile value, should be evaluated in addition to the RMSE. Each DEM is discussed in detail below.

WV1_DSM

Although the raw leaf-on DSM (figure 3C) captures the general topography of the study area it is noisy and smooths terrain complexity compared to the reference. From the profile view (figure 4), it is clear that the leaf-on WV1 DSM elevations generally lies between the reference DEM and the SRTM.

Quantitative error metrics suggest that the WV1_DSM is comparable to the SRTM in accuracy. Its mean error of 11.60 m is slightly lower than the 12.84 m mean error of the SRTM, however its RMSE of 13.68 m is slightly higher than the SRTM's 13.48 m RMSE. Of particular note, its non-normal distribution error values are greater than those of the SRTM (Table 6).

WV1_FIL

Simple filtering of the elevations classified as ground (method WV1_FIL) results in a DEM (figure 3D) that qualitatively appears to be an improvement on the photogrammetric DSM. The large maximum positive error is comparable to that of the SRTM, but the minimum error is large compared to that of the SRTM and indicates that the filtered DEM lies below the reference surface, at least in places. In evaluating terrain morphology of this filtered DSM, there are several high-elevation artifacts within the main stream valley caused by tall vegetation overhanging the stream. These artifacts function hydrologically as false dams and would result in poor modeling of water flow. Bowl-shaped depressions in this DEM are caused by actual ground elevations surrounded by unfiltered vegetation elevations, and are a second indication of the limited success of the simple filtering procedures.

Despite the visual presence of artifacts and outliers, the filtering decreases the amount of error present in the DSM by all metrics. Based on the low p-value result of the one directional Wilcoxon test (Table 7), the null hypothesis is rejected and the median error value of WV1_FIL is found to be significantly ($\alpha < 0.05$) less that of the unfiltered DSM, indicating the filtered DEM represents an improvement over the original data.

WV1_FIL2

The addition of a vertical offset to reduce the effect of vegetation artifacts (method WV1_FIL2) results in a DEM (figure 3E) with minimum and maximum elevations similar to the reference DEM. However the errors observed in the raw DSM and simple ground filtering (WV1_FIL), such as vegetation artifacts and sinks caused by low areas surrounded by vegetation, are still present (albeit reduced). New errors have been introduced where the vertical offset overcompensates for vegetation height and causes the filtered surface to be below the reference surface (figure 4). Thus, while the WV1_FIL2 generally lies close to the reference surface, it exhibits several areas of too high or too low elevation.

Despite these inconsistencies, the WV1_FIL2 is quantitatively the most accurate leaf-on DEM (Table 6), with the lowest RMSE, mean error and non-normal distribution metric values. Based on the results of the one-directional Wilcoxon follow-up test (see Table 8), the null hypothesis is rejected and the median error value of WV1_FIL2 is found to be significantly less than that of both the unfiltered DSM and WV1_FIL.

WV1_FIL3

The inclusion of a vertical offset based on stream proximity (method WV1_FIL3) produces a DEM (figure 3F) with substantially more terrain detail and a well-defined drainage pattern similar to the reference DEM. Despite a higher maximum value, qualitatively this method successfully reproduces the reference terrain (figure 4). Although it appears to be an improvement over the WV1_FIL2 method and improves the hydrologic functionality of the DEM, the RMSE, mean error, and non-normal distribution metric values for WV1_FIL3 are higher than those of WV1_FIL2 (Table 6). Furthermore, the Wilcoxon test results are somewhat contradictory for WV1_FIL3. The first test result (Table 8) indicates a rejection of the null hypothesis and confirms that the median value of WV1_FIL3 is significantly lower than that of the unfiltered DSM. However, the follow-up Wilcoxon test (Table 9) supports the acceptance of the null hypothesis that the median error of WV1_FIL3 is not significantly lower than that of the simple filtering (WV1_FIL). The latter result suggests that the simple vertical offset applied to all vegetation pixels of the WV1_FIL2 method produces a DEM with median error lower than is found for the DEM with the more complex offset designed to improve hydrologic flow (WV1_FIL3).

WV3_DSM and WV3_FIL

The leaf-off DEMs (figure 3G and 3H) are more successful in capturing the range of elevation and complexity of terrain features visible in the reference DEM. Elevation artifacts caused by stands of evergreen vegetation are clearly visible in the raw leaf-off DSM (figure 3G). These areas appear as contained areas of higher elevation than the surrounding terrain and are mostly removed by the filtering procedures (WV3_FIL). Qualitatively and quantitatively by all metrics, the filtered leaf-off DSM (figure 3H) is the most similar to the reference DEM.

Effect of Land Cover on Filtered DEMs

A positive correlation exists between canopy height and error in all leaf-on DSMs (Table 10), but the moderate strength of this relationship suggests that error magnitude in the DSMs (defined as difference from the DEM) is not entirely caused by the height of the vegetation canopy.

Results of the analysis of error by land cover class (figure 5), indicates that error differs substantially by land cover. The difference in error between different land cover categories is greatest in the leaf-on DEMs, but even in the leaf-off DEMs error varies notably between the different land cover classes. It is not surprising that the leaf-on WV1_DSM reflects the largest difference in error values between land cover categories, as this DSM is created at a scale and during the phenological state that best captures canopy differences. However, it should not be assumed that the leaf-on DSM represents a

perfect addition of the ground surface elevation and the height of vegetation canopy because the DSM does not consistently capture the upper canopy surface.

The additional importance of figure 5 lies in the isolation of the Open land cover category for all evaluated DEMs. Open areas of each DEM, including DSMs, are conceptually equivalent to a digital terrain model. Thus evaluation of the median error within Open areas compares the DEMs at their most accurate spots. In these areas of high accuracy it can be seen that WV1_FIL3 has the lowest median error, and thus is the closest leaf-on DEM to the reference terrain. WV1_FIL2 over-compensates for vegetation height, resulting in a negative median error. Both leaf off DEMs (WV3_DSM and WV3_FIL) also have negative median error, but the value is substantially smaller than that of WV1_FIL2. Based on this median error metric, WV3_DSM has the lowest error and thus most closely models the reference terrain. The land cover class exhibiting the greatest potential error in each DEM is either deciduous forest or evergreen forest, depending on the seasonality of source imagery. In the leaf-on DEMs, median error of the filtered DEMs is lower for both deciduous and evergreen classes, suggesting that filtering successfully reduces the artifacts of vegetation canopy. Of these DEMs, WV1_FIL2 exhibits the smallest median error values. In the leaf-off DSM median error is negative for both classes and increases as a result of filtering, but these values are small compared to those of the leaf-on DEMs.

Conclusion

This work evaluated how effectively lidar filtering techniques can be used to reduce the error in a digital surface model (DSM) derived photogrammetrically from high-resolution stereo satellite imagery in a densely forested environment. The central challenge in trying to generate a bare earth DEM from photogrammetric methods is the lack of ground returns from beneath the vegetation canopy. In this study, fine spatial resolution photogrammetric DSMs were extracted from stereographic WorldView imagery in leaf-on and leaf-off conditions, then converted to a LAS point cloud. Ground terrain was identified using lidar point classification methods and then interpolated to create a bare earth digital terrain model (DEM).

Overall it was found that a photogrammetric DSM may be created that is of similar spatial resolution to a lidar DEM, however the lack of multiple returns in the photogrammetric point cloud greatly limits the success of creating a bare-ground DEM in leaf-on forested land cover. Lidar processing techniques were partially successful in identifying points within the photogrammetric point cloud that fell upon the ground surface, but the fundamentally different 3D structure of the point cloud ultimately reduces the accuracy of the filtered DEM. Through filtering the effect of the vegetation canopy on the DSM elevation surface can be substantially diminished, creating a DEM with accuracy between that of the SRTM and a lidar bare earth DEM. The accuracy of the leaf-on filtered DEM created in this study would make it useful for terrain visualization and estimation of elevation, however it contains artifacts

that limit its use in hydrologic modeling applications. Subsequent smoothing may reduce the effect of such artifacts and improve hydrologic flow, but at the cost of the fine-scale terrain detail.

Filtering procedures were more successful in removing the vegetation artifacts from the leaf-off photogrammetric DSM. In this study, the raw DSM extracted from leaf-off stereo imagery was similar in vertical accuracy to the reference DEM and correctly modeled the complexity of terrain features with minimal noise. Furthermore, elevation artifacts from evergreen vegetation and other surface features were successfully removed using lidar filtering procedures, resulting in a bare earth DEM with an accuracy comparable to that a bare earth DEM created from lidar and useful for hydrologic modeling.

The findings of this study offer potential guidance for those considering the use of photogrammetric methods using high-spatial resolution imagery to generate DSMs in areas lacking high-resolution elevation data. The study area's leaf-on, deciduous forest land cover presents a challenge for the creation of a bare earth DEM, however the filtering procedures explored in this research significantly improved the accuracy and usability of each photogrammetric DSM. Additional research in this area should evaluate the potential of new filtering methods and point classification algorithms in different types of terrain and land cover.

References

Bühler, Y., M. Marty, and C. Ginzler. 2012. "High Resolution DEM Generation in High-Alpine Terrain Using Airborne Remote Sensing Techniques." Transactions in GIS 16 (5): 635–47. doi:10.1111/j.1467-9671.2012.01331.x.

Chirico, P., K. Malpeli, and S. Trimble. 2012. "Accuracy Evaluation of an ASTER-Derived Global Digital Elevation Model (GDEM) Version 1 and Version 2 for Two Sites in Western Africa." GIScience & Remote Sensing 49(6):775-801.

Dewberry. 2012. Project Report for the Virginia Counties North Acquisition and Classification for FEMA VA LiDAR.

DeWitt, J., T. Warner, and J. Conley. 2015. "Comparison of DEMS derived from USGS DLG, SRTM, a statewide photogrammetry program, ASTER GDEM and LiDAR: implications for change detection." GIScience & Remote Sensing 52(2): 179-197.

Elmore, A., S. Guinn, G. Sanders. 2013. "Vegetation structure within the National Capital Region Network using LiDAR data and analysis: Prince William Forest Park, Catoctin Mountain Park, C & O Canal National Historical Park, and Harpers Ferry National Historical Park." Natural Resource Data Series. NPS/NCRN/NRDS—2013/475. National Park Service. Fort Collins, Colorado.

Fisher, Peter F. and N. Tate. 2006. “Causes and Consequences of Error in Digital Elevation Models.” Progress in Physical Geography 30 (4): 467–89.

Gesch, D., M. Oimoen, and G. Evans. 2014. “Accuracy Assessment of the U.S. Geological Survey National Elevation Dataset, and Comparison with other Large-Area Elevation Datasets – SRTM and ASTER.” U.S. Geological Survey Open-File Report 2014-1008, 10p. http://dx.doi.org/10.3133/ofr20141008.

Höhle, J., and M. Höhle. 2009. “Accuracy Assessment of Digital Elevation Models by Means of Robust Statistical Methods.” Isprs Journal of Photogrammetry and Remote Sensing 64: 398–406. doi:10.1016/j.isprsjprs.2009.02.003.

Leberl, F., A. Irschara, T. Pock, P. Meixner, M. Gruber, S. Scholz, and A. Wiechert. 2010. “Point Clouds: Lidar versus 3D Vision.” Photogrammetric Engineering & Remote Sensing 76 (10): 1123–34. doi:0099-1112/10/7610–1123.

Maxwell, A., and T. Warner. 2015. “Differentiating mine-reclaimed grasslands from spectrally similar land cover using terrain variables and object-based machine learning classification.” International Journal of Remote Sensing 36(17): 4384-4410. DOI: 10.1080/01431161.2015.1083632.

Maxwell, A., T. Warner, and M. Strager. 2016. Predicting Palustrine Wetland Probability using Random Forest Machine Learning and Digital Elevation Data-Derived Terrain Variables. Photogrammetric Engineering and Remote Sensing 82(6): 437-447. doi: 10.14358/PERS.82.6.437.

Meng, X., N. Currit, and K. Zhao. 2010. “Ground Filtering Algorithms for Airborne LiDAR Data: A Review of Critical Issues.” Remote Sensing 2 (3): 833–60. doi:10.3390/rs2030833.9iojhhjjkl

Mongus, D., and B. Žalik. 2012. “Parameter-Free Ground Filtering of LiDAR Data for Automatic DTM Generation.” ISPRS Journal of Photogrammetry and Remote Sensing 67 (1): 1–12. doi:10.1016/j.isprsjprs.2011.10.002.

Montealegre, A., M. Lamelas, and J. De Riva. 2015. “A Comparison of Open-Source LiDAR Filtering Algorithms in a Mediterranean Forest Environment.” IEEE Journal of Selected Topics in Applied Earth Observations and Remote Sensing 8 (8): 1–14.

Müller, J., I. Gärtner-Roer, P. Thee, and C. Ginzler. 2014. “Accuracy Assessment of Airborne Photogrammetrically Derived High-Resolution Digital Elevation Models in a High Mountain Environment.” ISPRS Journal of Photogrammetry and Remote Sensing 98 (October 2015): 58–69. doi:10.1016/j.isprsjprs.2014.09.015.

Ni, W., K. Ranson, Z. Zhang, and G. Sun. 2014. “Features of Point Clouds Synthesized from Multi-View ALOS/PRISM Data and Comparisons with LiDAR Data in Forested Areas.” Remote Sensing of Environment 149. Elsevier Inc.: 47–57. doi:10.1016/j.rse.2014.04.001.

Novoa, J., K. Chokmani, R. Nigel, and P. Dufour. 2015. “Quality Assessment from a Hydrologic Perspective of a Digital Elevation Model Derived from WorldView-2 Remote Sensing Data.” Hydrological Sciences Journal 60 (2): 131217034946009. doi:10.1080/02626667.2013.875179.

Passini, R., D. Betzner, and K. Jacobsen. 2002. “Filtering of Digital Elevation Models.” In ASPRS Annual Convention, Washington, 9.

Sefercik, U., M. Alkan, G. Buyuksalih, and K. Jacobsen. 2013. “Generation and Validation of High-Resolution DEMs from Worldview-2 Stereo Data.” Photogrammetric Record 28 (144): 362–74. doi:10.1111/phor.12038.

Sithole, G., and G. Vosselman. 2004. “Experimental Comparison of Filter Algorithms for Bare-Earth Extraction from Airborne Laser Scanning Point Clouds.” ISPRS Journal of Photogrammetry and Remote Sensing. doi:10.1016/j.isprsjprs.2004.05.004.

Tarolli, P. 2014. “Geomorphology High-Resolution Topography for Understanding Earth Surface Processes : Opportunities and Challenges” 216: 295–312.

Thornberry-Erlich, T. 2009. “Prince William Forest Park Geologic Resources Inventory.” Report. Natural Resource Report NPS/ NRPC/ GRD/ NRR – 2009/086. National Park Service, Denver, CO.

Wilson, J. 2012. “Digital Terrain Modeling.” Geomorphology 137 (1). Elsevier B.V.: 107–21. doi:10.1016/j.geomorph.2011.03.012

Tables

Table 1. Data used in the study

Satellite/ Source	Date (Season)	View Type	Characteristics	Pixel size (m)	Used For
Digital Imagery					
WorldView1	2015 Oct 10 (Leaf on)	Stereo	Panchromatic	0.5	Photogrammetric DSM
WorldView3	2015 Oct 6 (Leaf on)	Mono	Multispectral - 4 band (VIS-NIR)	1.5	Classification of land cover
WorldView3	2016 Mar 7 (Leaf off)	Stereo	Panchromatic	0.5	Photogrammetric DSM
Aerial orthoimagery	2013 Spring (Leaf off)	Ortho-projected	Multispectral - 4 band (VIS-NIR)	0.3	Accuracy assessment of Land cover classification
Digital Elevation Data					
NED 1/9 arc sec	Not Available	Not Applicable	Bare earth DEM	3	Reference DEM
SRTM	2000 February	Not Applicable	DEM	30	Globally available DEM data
Raw lidar data	2011	Not Applicable	LAS point cloud	(5 pts/m^2)	Photogrammetric to lidar point cloud comparison

Table 2. Software used in this study, categorized by analysis task.

Analysis Task	Software	Additional Licenses
1. Land cover classification	ArcGIS 10.1	Image Classification toolbar
2. DSM extraction	PCI Geomatica	Focus and OrthoEngine
3. LAS point classification	GlobalMapper 17.1	Lidar extension
4. LAS interpolation to DEM	ArcGIS 10.1	Spatial Analyst
5. DEM comparison	ArcGIS 10.1	Spatial Analyst

Table 3. DSMs produced from the tested filtering methods

Name	**Procedures (in order of completion from left to right)**					
	Convert to point cloud	Noise Filter	Ground Classification	Vegetation Classification and 10 m offset	10 m offset of points within 5 m of the streamline	Interpolation
Leaf On DSM						
WV1_DSM						
WV1_FIL	X	X	X			X
WV1_FIL2	X	X	X	X		X
WV1_FIL3	X	X	X		X	X
Leaf Off DSMs						
WV3_DSM	X					
WV3_FIL	X	X	X			X

Table 4. Number of points randomly distributed within each category of land cover.

Land Cover Category	Coverage Area	No. of Points
Open/ field	5.3%	53
Evergreen Forest	23.8%	238
Deciduous Forest	70.9%	709

Table 5. Average area of TIN triangle facets.

Area metric (m2)	WV1_DSM Ground points	Lidar Ground Points
Min	0.0	0.0
Maximum	1,801.6	262.3
Mean	2.3	0.2

Table 6. Results of DEM error analysis. Descriptive statistics of signed error and absolute error, as well as normal distribution accuracy metrics and non-normal distribution accuracy metrics are given for each DEM evaluated in the study.

		SRTM	WV1_DSM	WV1_FIL	WV1_FIL2	WV1_FIL3	WV3_DSM	WV3_FIL
Descriptive Statistics								
Signed Error	Maximum (m)	26.62	28.77	22.13	17.07	22.19	25.61	4.47
	Minimum (m)	0.68	-16.77	-16.59	-22.53	-23.94	-4.90	-7.91
	Mean (m)	12.84	11.60	6.68	0.40	6.69	0.46	-0.71
	Std. Dev (m)	4.11	7.25	6.94	6.90	7.19	3.77	1.05
	Skewness (m)	0.17	-0.66	-0.52	-0.43	-0.64	4.91	-2.33
Absolute Error	Maximum (m)	26.62	28.77	22.13	22.53	23.94	25.61	7.91
	Minimum (m)	0.68	0.02	0.03	0.01	0.00	0.00	0.00
	Mean (m)	12.84	12.23	8.18	5.57	8.35	1.40	0.84
	Std. Dev (m)	4.11	6.13	5.08	4.09	5.16	3.53	0.94
Normal Distribution Accuracy Metrics								
	RMSE (m)	13.48	13.68	9.63	6.91	9.82	3.79	1.26
Accuracy Metrics – No Assumption of Normality								
	50^{th} percentile (m)	12.76	12.42	7.18	1.00	7.19	-0.38	-0.56
	68.30^{th} percentile (m)	14.62	15.35	10.54	3.97	10.66	-0.05	-0.31
	95^{th} percentile (m)	19.70	22.30	17.09	10.74	17.29	3.87	0.45
	NMAD (m)	4.09	7.29	10.51	9.46	12.13	0.61	0.91

Table 7. Wilcoxon test of median error values

DEM	Estimated	Confidence Interval (m)	
	Median (m)	Lower	Upper
WV1_DSM	11.96	11.51	12.41
WV1_FIL	6.96	6.55	7.43
WV1_FIL2	0.66	0.22	1.10
WV1_FIL3	7.07	6.62	7.52

Table 8. Wilcoxon one directional test of median error values (less than the 11.96 m estimated median of WV1_DSM).

DEM	Estimated Median (m)	Wilcoxon Statistic	P-Value
WV1_FIL	7.00	68507.0	0.000
WV1_FIL2	0.66	1439.0	0.000
WV1_FIL3	7.07	72591.0	0.000

Table 9. Wilcoxon one directional test of median error values (less than the 6.995 m estimated median of WV1_FIL).

DEM	Estimated Median (m)	Wilcoxon Statistic	P-Value
WV1_FIL2	0.66	40058.0	0.000
WV1_FIL3	7.07	253238.0	0.628

Table 10. Correlation coefficients for the error in each DEM (calculated as DEM minus NED) and the canopy height raster created from lidar.

DEM	Correlation Coefficent
WV1_DSM	0.595
WV1_FIL	0.431
WV1_FIL2	0.486
WV1_FIL3	0.424
WV3_DSM	-0.053
WV3_FIL	-0.057

Table 11. Confusion matrix for land cover classification. Overall Accuracy is 85%.

		Reference Image				User's
		Field/ Open	**Evergreen**	**Deciduous**	**Total**	**Accuracy**
Classified Image	**Field/ Open**	14	4	14	32	44%
	Evergreen	4	67	50	121	55%
	Deciduous	6	39	277	322	86%
	Total	24	110	341	**358**	
	Producer's Accuracy	58%	61%	81%		

Figures

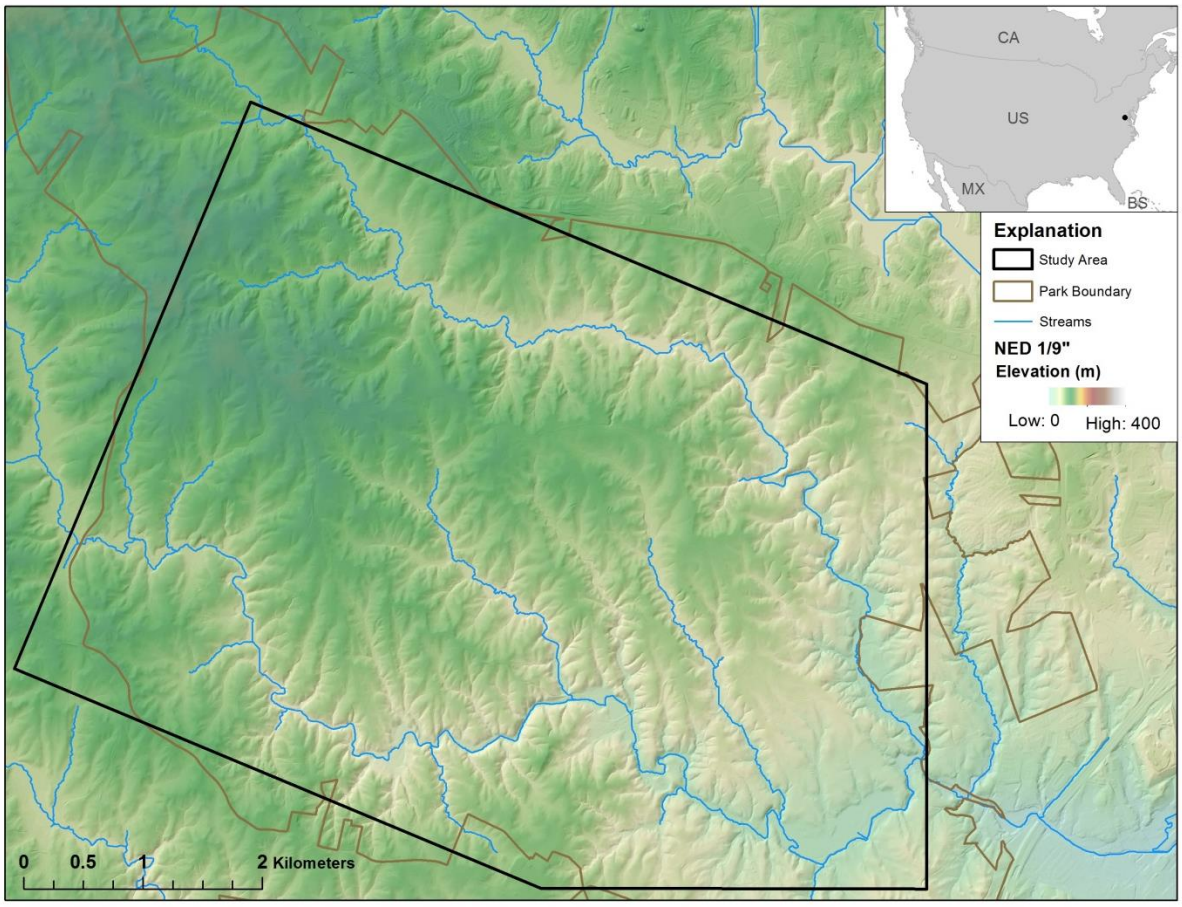

Figure 1. Study area within Prince William Forest Park in Prince William County, Virginia, USA. Mapped on Worldview-3 visible bands 5-red, 3-green, 2-blue, collected on October 6, 2014.

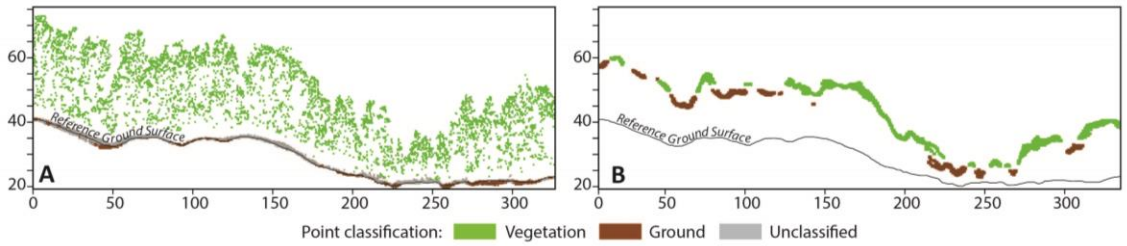

Figure 2. The 3D structure of the lidar point cloud (A) is inherently different than that of the photogrammetrically derived point cloud (B). Point classification using lidar techniques accurately identifies ground and vegetation points within the lidar dataset (A), but may not correctly differentiate between the two in the photogrammetrically derived dataset. Moreover, the elevation of vegetation point areas in the photogrammetric point cloud (B) must be interpolated from the closest ground point values.

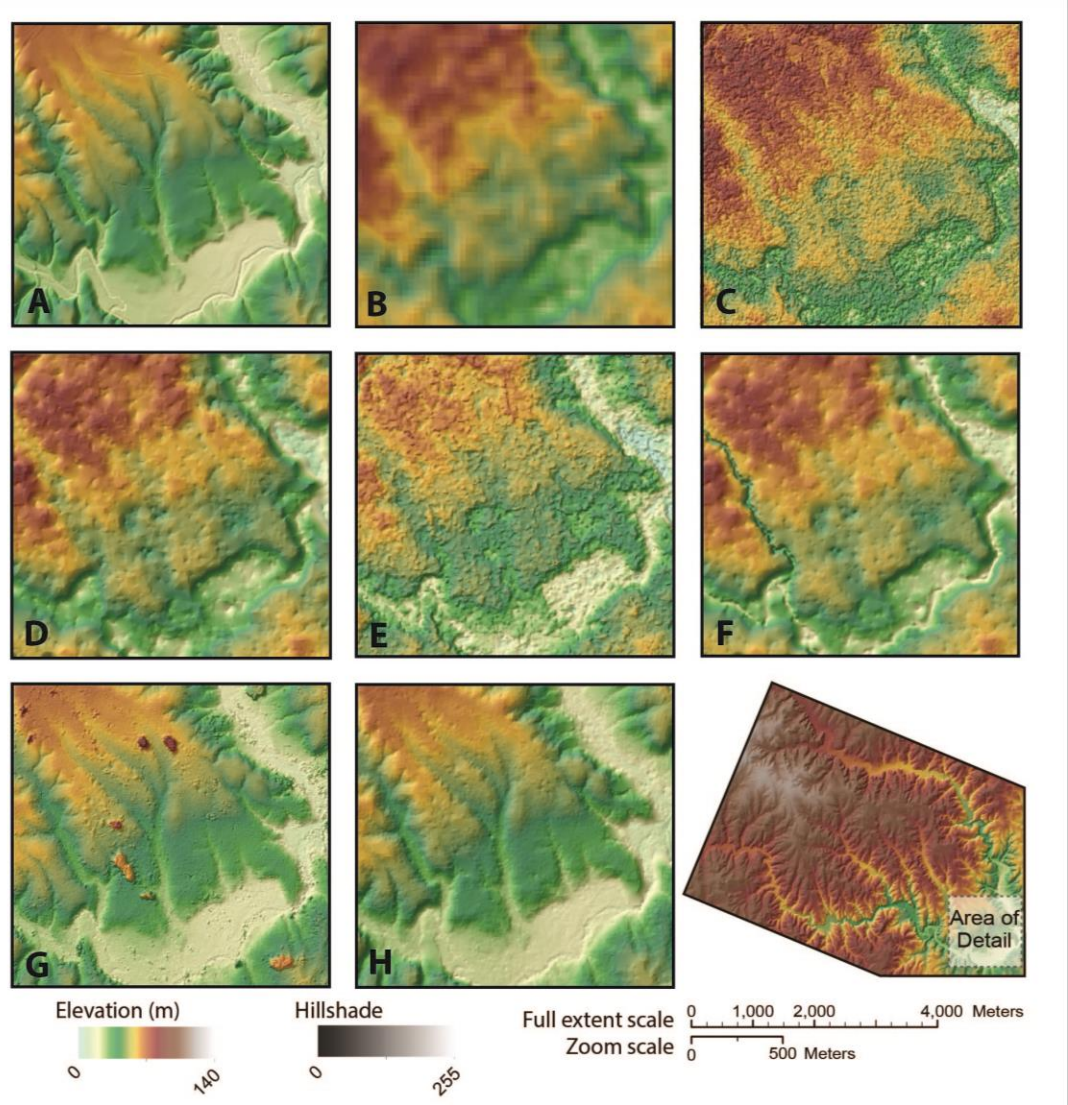

Figure 3. Visual comparison of DEMs: A) reference digital terrain map (from the NED); B) 30m SRTM; C) raw digital surface model from leaf on WV1 imagery (WV1_DSM); D) filtered DSM (WV1_FIL); E) filtered leaf on DSM with vertical offset for tall vegetation (WV1_FIL2); F) filtered leaf on DSM with vertical offset for near-stream points (WV1_FIL3); G) raw DSM from leaf off WV3 imagery (WV3_DSM); and H) filtered leaf-off DSM (WV3_FIL).

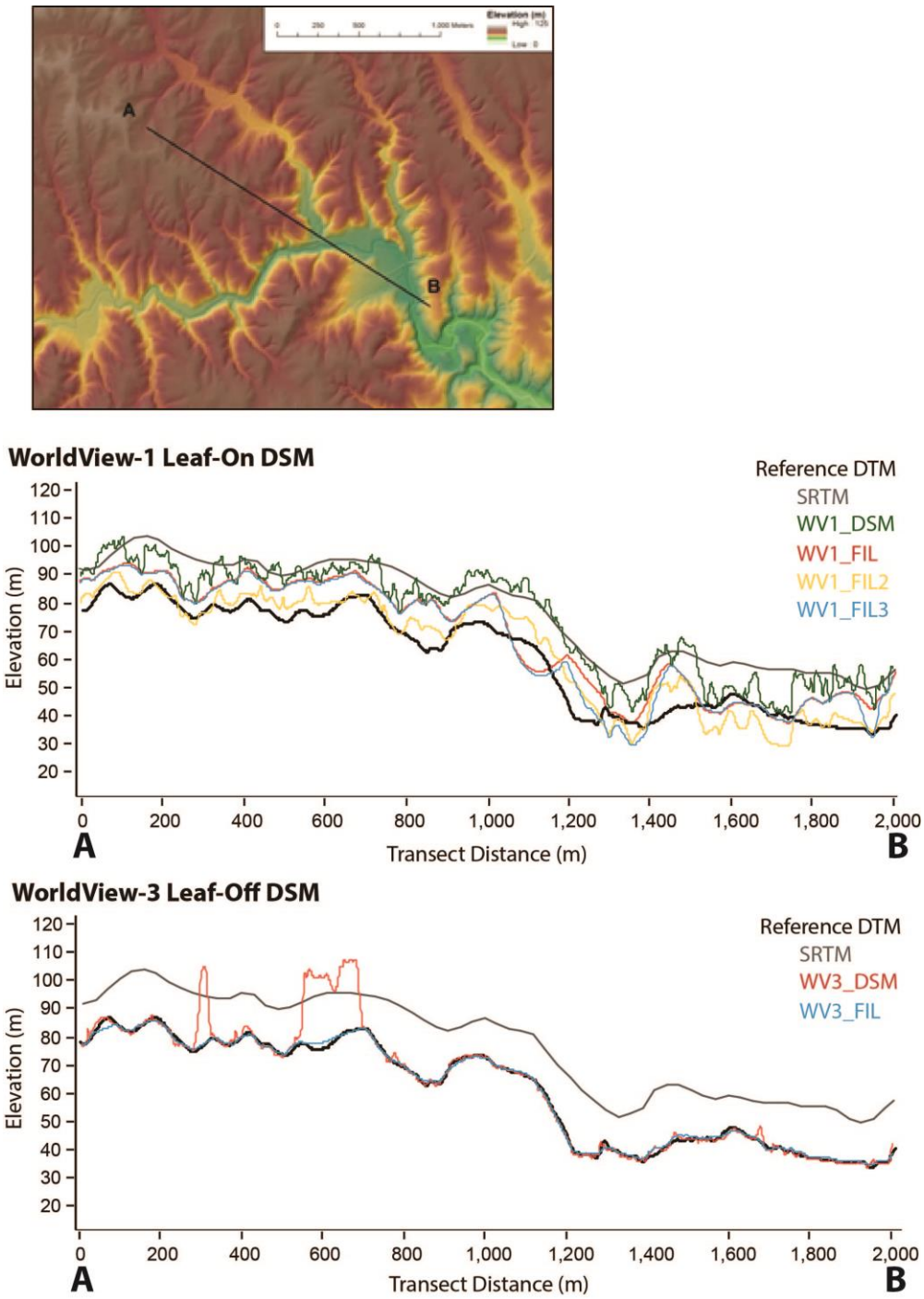

Figure 4. Profile comparison of DEMs. The map shows the transect location. The WorldView-1 Leaf-On DSM graph (top) compares the surface of WV1_DSM (green), WV1_FIL (red), WV1_FIL2 (yellow), and WV1_FIL3 (blue), with the reference DEM (black heavy line) and the SRTM (gray line). The WorldView-3 Leaf-Off DSM graph (bottom) compares the surfaces of WV3_DSM (red) and WV3_FIL (blue), with the reference DEM (black heavy line) and the SRTM (gray line) for the same transect.

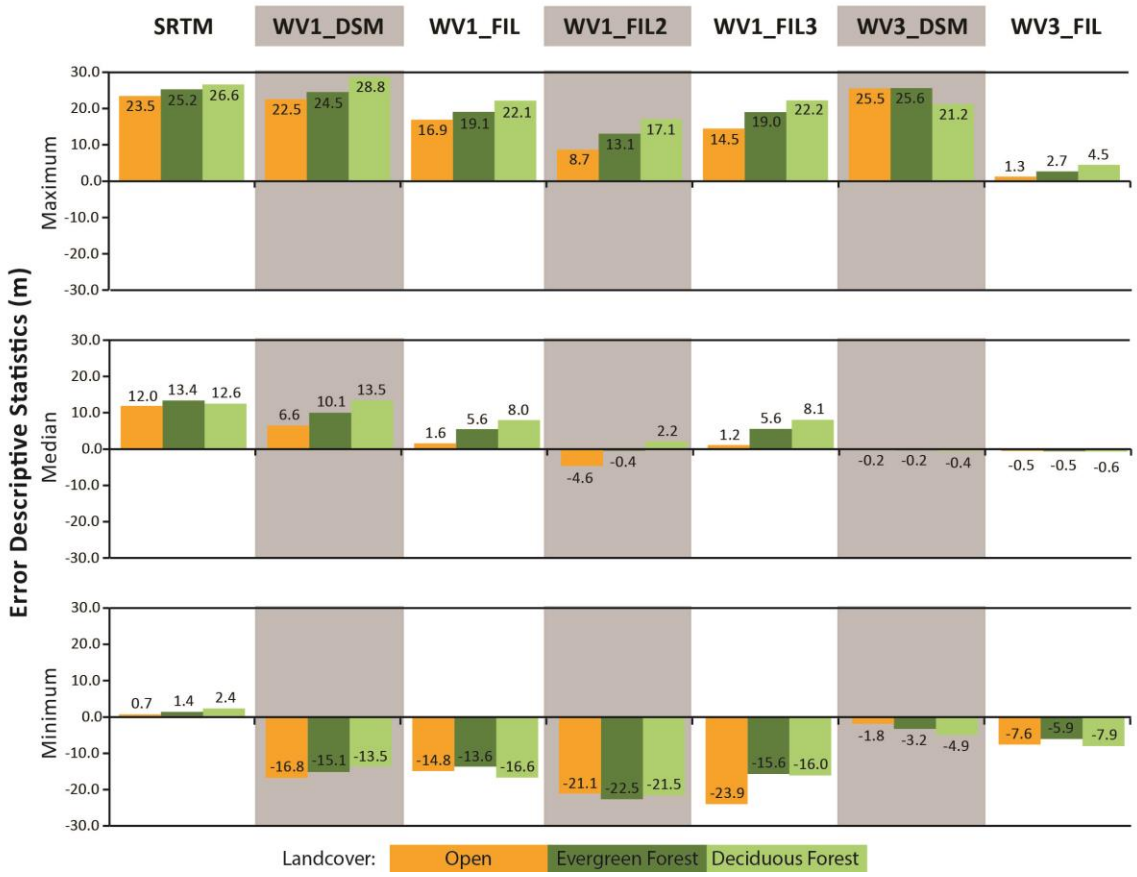

Figure 5. Error descriptive statistics for each DEM (m), presented by land cover.

Chapter 5 Conclusion

Summary and Synthesis

The papers presented in Chapters 2-4 have investigated specific challenges in the mapping and multi-dimensional monitoring of different scales of surface mining through remote sensing methods. This chapter summarizes the overall findings from all three papers, and discusses the potential implications for applied studies of surface or artisanal mining.

The challenge of mapping different scales of land use land cover (LULC) in an area of industrial and artisanal mining using remote sensing methods was explored in Chapter 2. This chapter described a method of independently analyzing LULC at regional- and local- scales, then subsequently integrating these analyses in order to comprehensively assess changes in the spatial distribution of fine-scale artisanal mining activity within the scope of changing regional land covers. Regional-scale LULC classification of Landsat using support vector machines allowed for mapping of spatially relevant land covers from 1984-2014. This classification successfully differentiated between some spectrally similar classes (such as tree crops and forest), but was less successful with others (such as mining/ bare and urban). Fine-scale artisanal mining LULC was then manually interpreted from high-resolution imagery for 2007 and 2014. These mining sites were compared to the regional-scale LULC classifications, and from this comparison it was clear that most ASM pits were located within the mixed vegetation class, suggesting that artisanal mining land use is generally not captured by Landsat multispectral classification in this environment. The small average size of an ASM pit (< 9% the size of a Landsat 30 m pixel) and the mixed land cover that occurs in close proximity to ASM pits are two factors that influence this misclassification. Integration of the fine-scale and regional-scale LULC analyses allowed for the accurate mapping of the distribution of both small and large areas of mining/ bare LULC. Although the inclusion of artisanal mining did not greatly increase the total area covered by the mining/ bare class, it altered the spatial distribution of this class – an important factor for community- and state- level management and monitoring.

The findings of this paper confirm the importance of fine-scale analysis in areas of artisanal mining and present a simple and widely applicable method to integrate multi-scalar, multi-source remote sensing analyses in order to map two very different types of mining. Not only does this method allow for analysis of the distribution of mining activity, but it also allows for comprehensive assessment of changes in other, interrelated land covers, such as urban area, forest, and agriculture that surround mining regions.

Quantification of landscape changes in the third dimension (topographic change) is also necessary in areas of resource extraction for applications such as the estimation of excavated volume and remaining mineral resources, modeling of hydrologic changes, and estimation of environmental impacts.

Topographic change calculated from DEM differencing is useful for such applications, but digital elevation models (DEMs), particularly globally available DEMs, differ widely in terms of their collection procedures, resolutions, and accuracies.

Chapter 3 focuses on the potential *accuracy* of topographic change estimates over time through investigation of the source data and accuracies of available DEMs. This study was performed in a relatively undisturbed (by mining) part of southern West Virginia, USA. Most DEM descriptions typically include only a single accuracy metric (typically the root mean squared error (RMSE)), which is not regionally specific and does not describe the spatial distribution of error across the landscape. In the study, error was assessed in the available DEMs through comparison to a lidar bare-earth DEM. The results of this comparison called attention to the significantly large, positive, and normally distributed errors of both the shuttle radar topography mission (SRTM) and the Aster Global DEM (GDEM), indicating that terrain modeled by each of these DEMs is consistently above that of the reference DEM. This finding was not unexpected, as these two DEMs are known to include some portion of the vegetation canopy in their elevation values. The other DEMs evaluated had low errors and more closely modeled the reference terrain. Ordinary least squares (OLS) regression testing of the relationship between error and elevation, slope, and aspect returned mixed results, suggesting that their modeled terrain surfaces differ substantially and may not be directly comparable.

The implications of these findings point to the limits on estimations of topographic change using moderate resolution DEMs. Although it is common to think of the DEM as the ground surface, plus or minus a single error metric (such as RMSE), the reality is that DEMs quantify the ground surface in different and complicated ways. Error is not uniform across this surface, and is likely autocorrelated, heteroskedastic, and at least partially dependent on land cover. Topographic change estimates require error bars that include the specific accuracies of the DEMs used to quantify change. At the very least, values of ±RMSE of each DEM should be considered, and amounts of change smaller than this combined error may appear as 'noise' and therefore not be quantified as change. The amount and spatial distribution of error in both the SRTM and the GDEM suggests that neither is comparable to the other DEMs evaluated, particularly since the GDEM is not associated with a specific moment in time and could therefore introduce additional error to topographic change quantification. Unfortunately, these two DEMs may be the only elevation datasets available for international areas of interest. The take-home message from this case study of topographic change in industrial mining areas is that a better DEM is necessary for the quantification of smaller magnitudes of change, such as that which occurs in areas of artisanal mining.

The challenge of mapping fine-scale topographic changes in remote- or data-scarce areas such as those involved in artisanal mining is addressed in Chapter 4. This chapter presents a method of creating and filtering surface feature artifacts from fine-spatial resolution, globally available photogrammetric

digital surface models (DSMs). Although the raw photogrammetrically created DSM was found to have a RMSE greater than the SRTM, in many areas its modeled surface existed between that of the SRTM and the reference DEM. The presence of elevation artifacts caused by surface features not only reduced the accuracy of the terrain modeled by the DSM, but also impeded hydrologic analysis using the DEM. A bare-earth DEM was created through conversion of the DSM to lidar format (.las) point clouds, classification of the points as ground or vegetation, and subsequent filtering of non-ground points. In leaf-on conditions, the ground filtering procedures significantly improved the RMSE, along with additional procedures of negative vegetation offset. Despite these improvements, correct hydrologic flow was not achieved due to the presence of dense vegetation in stream valleys, which limited the number and distribution of ground points. Vertical offset of vegetation in close proximity to the stream did not improve the RMSE, but did result in a more hydrologically functional DEM. In leaf-off conditions, the ground filtered DEM achieved low RMSE and correct hydrologic flow paths, successfully approximating the bare-earth reference DEM. These results indicate that this method could be used to create an approximation of a bare-earth DEM where no lidar data is available. Although the presence of large areas of dense vegetation canopy could negatively influence the RMSE of such a DEM, this work suggests that the filtered DEM would still be an improvement over the SRTM. Future research will entail evaluation of this method in mixed-LULC and will evaluate the degree to which small-scale changes in topography are captured by the ground filtered photogrammetric DEMs. Furthermore, 4D mapping, integrating high-resolution LULC classification with high resolution DSMs, could allow for improvement of filtering procedures to include spectral characteristics.

Final Remarks

Mapping and monitoring of resource extraction sites over time is important not only for the quantification of LULC and topographic change, but also in the assessment of the multitude of environmental impacts that result from mining. Remote sensing and geographic information systems (GIS) are two geospatial tools that enable the systematic and repeatable mapping of mining-related change. However, there are many challenges associated with the remote sensing of mining, determined by the scale of mining and the dimensionality of analysis, and potentially further exacerbated by paucity of data in remote mining regions. In general moderate-resolution imagery and DEMs, such as Landsat and the SRTM can be used to map industrial-scale mining, but fine spatial resolution is necessary for artisanal and small-scale mining activity. However, in the analysis of topographic change over time, even moderate-scale DEMs may have insufficient accuracy for the quantification of industrial-scale elevation changes. In remote regions lacking access to lidar, photogrammetric DSMs produced from high-spatial resolution stereo satellite

imagery have great potential, particularly when paired with surface feature filtering methods, to fill the need for high quality elevation data.